# Stagnant Slab: A Review

Yoshio Fukao,[1] Masayuki Obayashi,[1]
Tomoeki Nakakuki,[2] and the Deep Slab Project Group*

[1]Institute for Research on Earth Evolution, Japan Agency for Marine-Earth Science and Technology, 2-15 Natsushimacho, Yokosuka, 237-0061, Japan; email: fukao@jamstec.go.jp

[2]Department of Earth and Planetary Systems Sciences, Graduate School of Science, Hiroshima University, 1-3-1 Kagamiyama, Higashi-Hiroshima, 739-8526, Japan; email: nakakuki@hiroshima-u.ac.jp

*Deep Slab Project Group: Hisashi Utada, Daisuke Suetsugu, Tetsuo Irifune, Eiji Ohtani, Shoichi Yoshioka, Hajime Shiobara, Toshihiko Kanazawa, and Kei Hirose.

Annu. Rev. Earth Planet. Sci. 2009. 37:19–46

First published online as a Review in Advance on January 15, 2009

The *Annual Review of Earth and Planetary Sciences* is online at earth.annualreviews.org

This article's doi:
10.1146/annurev.earth.36.031207.124224



0084-6597/09/0530-0019$20.00

## Key Words

subduction, mantle dynamics, tomography, mantle discontinuity

## Abstract

A stagnant slab is a subducted slab of oceanic lithosphere subhorizontally deflected above, across, or below the 660 km discontinuity. This phenomenon has now been widely recognized beneath subduction zones around the circum-Pacific and in the Mediterranean. Collaboration of seismic and electromagnetic observations, mineral physics measurements, and geodynamic modeling has begun to provide a consistent picture of stagnant slab.

## INTRODUCTION

Near-horizontal deflection of subducted slab was first detected from a traveltime analysis by Okino et al. (1989) and imaged in the transition zone beneath Japan by van der Hilst et al. (1991, 1993) and Fukao et al. (1992), through their P-wave traveltime tomography. Fukao et al. (1992) showed that such deflection or flattening occurs either above (as in Japan) or below (as in Indonesia) the 660 km discontinuity in the western Pacific. Fukao et al. (2001) made an extensive review of tomographic models of deeply seated slabs around the circum-Pacific to conclude that subducted slabs generally tend to be, once horizontally flattened at various depths, roughly between 400 and 1000 km. They referred to slabs with this tendency as stagnant slabs. The subsequent development in this direction includes imaging of the flattened slab of the Mediterranean lithosphere in the transition zone under southern Europe (Piromallo & Morelli 2003, Marone et al. 2004, Schmid et al. 2006), the Cocos-Farallon plate under southern Mexico (Gorbatov & Fukao 2005), and the remnant flattened slab of the Farallon plate under southern North America (Van der Lee & Nolet 1997, Schmid et al. 2002, Lei & Zhao 2006).

**Figure 1** shows a wide-angle slice of the P-wave tomographic model of the Earth's mantle (Fukao et al. 2001). This slice displays the stagnant slab of the Pacific plate behind the Honshu arc, which apparently lies on the 660 km discontinuity. The lowermost mantle under this stagnant

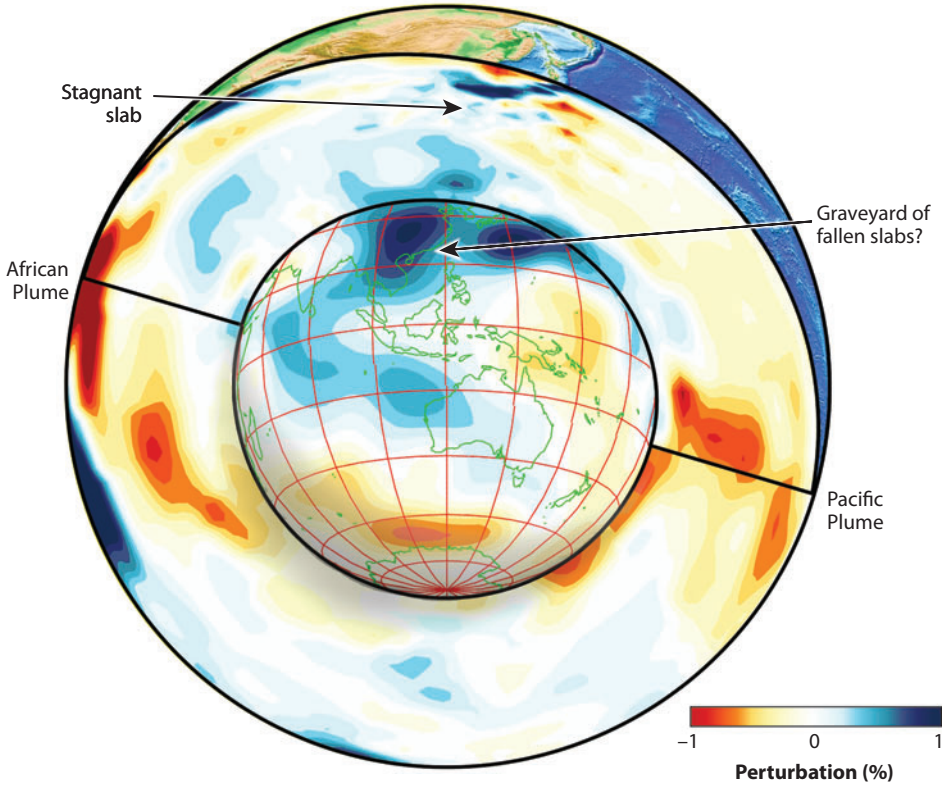


**Figure 1**

A wide-angle slice of the P-wave tomographic model of the Earth's mantle (Fukao et al. 2001), showing the stagnant slab of the Pacific plate behind the Honshu arc and the probable slab remnants in the deepest lower mantle.

slab image is marked by extensive high-velocity anomalies. The deepest of these anomalies, from the northwestern Pacific to eastern Eurasia, have been interpreted as the remnants of subducted slabs once falling through the lower mantle and now residing in the deepest lower mantle (Fukao et al. 1992, van der Voo et al. 1999). The Tethyan lithosphere (Grand et al. 1997, van der Hilst et al. 1997, Bijwaard et al. 1998, Replumaz et al. 2004, Hafkenscheid et al. 2006) and the Farallon lithosphere (Grand et al. 1997, van der Hilst et al. 1997, Bijwaard et al. 1998, Zhao 2004, Lei & Zhao 2006) are two obvious examples of subducted slabs that are now falling through the lower mantle but have not yet reached its bottom.

Our review addresses the following questions: How thermally and compositionally anomalous is a stagnant slab? Why does a subducted slab tend to be flattened once above or below the 660 km discontinuity? What happens to a slab that falls into the lower mantle?



## STAGNANT SLAB IMAGE BEHIND THE JAPANESE ARC

Because of the abundant seismic stations available in Japan and China, the stagnant slab behind the Japanese arc is ideally situated to obtain details of its fine structure. By adding the regional P-wave traveltime data of the Chinese networks to those reported to the International Seismological Center (ISC), Huang & Zhao (2006) were able to obtain sharper images of the flat portion of the Pacific slab under eastern China. **Figure 2** shows the east-west vertical cross sections of P-wave velocity perturbations along latitudes 43°, 39°, and 30°. The subducted slab of the Pacific plate is sharply deflected to horizontal when it hits the bottom of the upper mantle. The horizontal slab extends over a distance of 800 to 1000 km in the transition zone along the 660 km discontinuity. The uppermost mantle is significantly slow not only directly above the inclined Wadati-Benioff zone but also continentward, all the way above the horizontally deflected slab. Lei & Zhao (2005) and Huang & Zhao (2006) called this extensive low-velocity zone a "big wedge mantle" and emphasized its significance on surface tectonics, including intraplate seismicity and volcanism in eastern China. They suggested that water could be a messenger from the stagnant slab to the big wedge mantle. The possible presence of water has been indicated by a long-period magnetotelluric study (Ichiki et al. 2006) in a part of the upper mantle just above the stagnant slab of the same region.

Fukao et al. (2001) pointed out that the P-wave high-velocity images of stagnant slab from traveltime tomography can be compared with the broad spreads of S-wave high-velocity anomaly at the corresponding depths in long-wavelength tomographic models from waveform inversion, such as S12WM13 of Su et al. (1994) and SAW12D of Li & Romanowicz (1996). Such broad spatial similarity between the positive P- and S-wave velocity anomalies in the transition zone has also been pointed out by Grand (2002) and Romanowicz (2003). To date, however, high-resolution tomographic studies using S-wave traveltime data have not yielded stagnant slab images comparable in sharpness and intensity to those from P-wave tomography. Widiyantoro et al. (1999) made a joint inversion of P- and S-wave travel times by selecting data that have a common source and receiver for P and S arrivals. Their models showed substantial differences in the stagnant slab image between the P- and S-wave tomography. For example, the P-wave image beneath the Izu-Bonin region showed a strong signature of stagnant slab, but the S-wave image did not. This point has been elaborated by Gorbatov & Kennett (2002) and Kennett & Gorbatov (2004), who made joint tomography for bulk-sound and shear wave velocities using arrival times for paths with a common source and receiver for P and S. **Figure 3** displays the vertical cross section through the model of Gorbatov & Kennett (2002) across the Izu-Bonin and Ryukyu arcs along profile PP′ within the map in **Figure 2**. The downgoing part of the subducted slab is strongly anomalous in shear wave velocity but only slightly anomalous in bulk-sound velocity, whereas

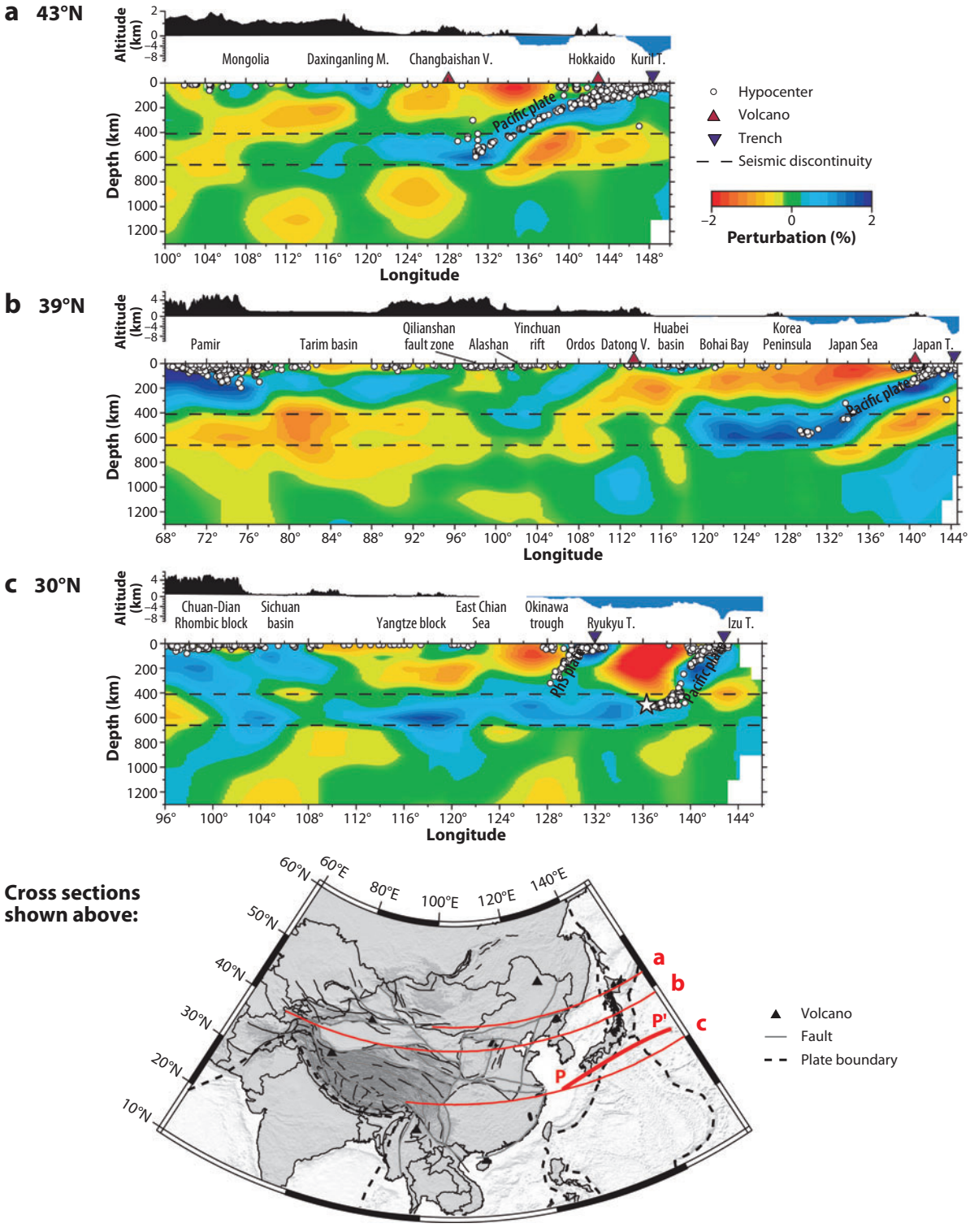

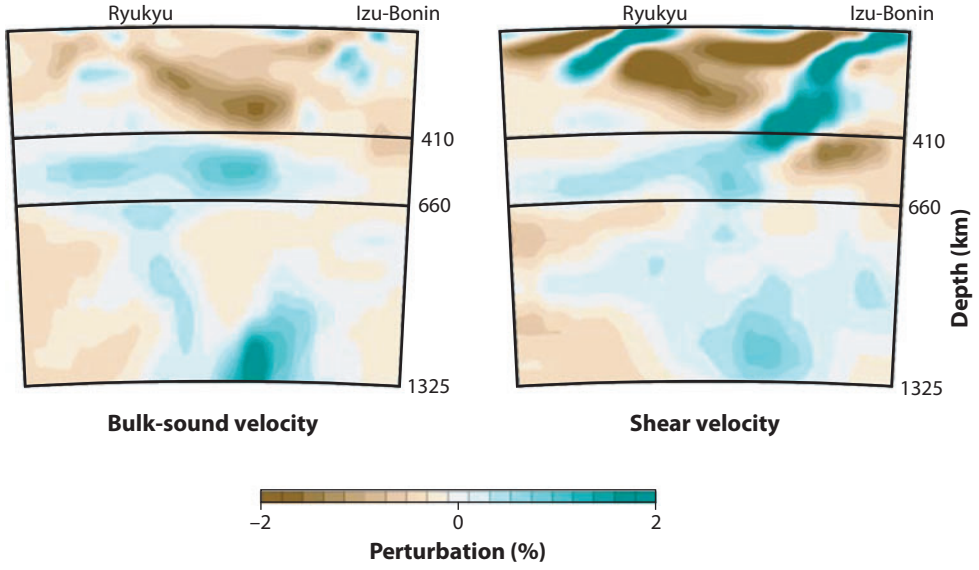


**Figure 3**

Vertical cross sections of bulk-sound velocity and shear velocity anomalies across the Izu-Bonin and Ryukyu arcs along profile PP′ in the map of **Figure 2** [Gorbatov & Kennett (2002), with permission from Elsevier]. The downgoing part of the subducted slab is strongly anomalous in shear velocity but only slightly anomalous in bulk-sound velocity, whereas the horizontal portion is more anomalous in bulk-sound velocity than in shear velocity.

the horizontal portion is more anomalous in bulk-sound velocity than in shear velocity. This may imply that the thermal anomaly controls velocity anomalies of the downgoing portion, and the compositional difference contributes significantly to the anomalies of the horizontal portion (Gorbatov & Kennett 2002).

There is, however, some evidence that the horizontal portion is anomalously fast not only in P but also in S by such amounts as expected from the thermal effect. **Figure 4** shows the vertical P and transverse S broadband seismograms at stations in southwestern Japan and China for the deep shock of June 3, 2002 that occurred at a depth of 494 km within the Izu-Bonin slab. (See **Figures 2** and **5** for the hypocenter.) In a distance range in which the effect of the stagnant slab is significant, the visually identified P arrivals are significantly early relative to the reference travel-time curve of IASP91 (Kennett & Engdahl 1991) and are in good agreement with those predicted from the three-dimensional (3D) P-wave model of Obayashi et al. (2006) (Sugioka et al. 2007). This model is converted to a 3D S-wave model using the P-to-S velocity ratio of IASP91 for the 1D part and choosing an appropriate value of $R = (dVs/Vs)/(dVp/Vp)$ for the laterally perturbed part, where $dVp/Vp$ and $dVs/Vs$ are fractional P and S velocity perturbations (Karato, 1993, Masters et al. 2000, Bolton & Masters 2001). The resultant theoretical S arrivals are in good agreement with the

**Figure 2**

East-west vertical cross sections of P-wave velocity perturbations along latitudes 43°, 39°, and 30°, where the horizontal slab (i.e., stagnant slab) extends over a distance of 800 to 1000 km above the 660 km discontinuity. Modified with permission from Huang & Zhao (2006). Line PP′ in the map is the profile for the cross sections in **Figure 3**. The star in (*c*) denotes the hypocenter of a deep shock relevant to **Figure 4**.

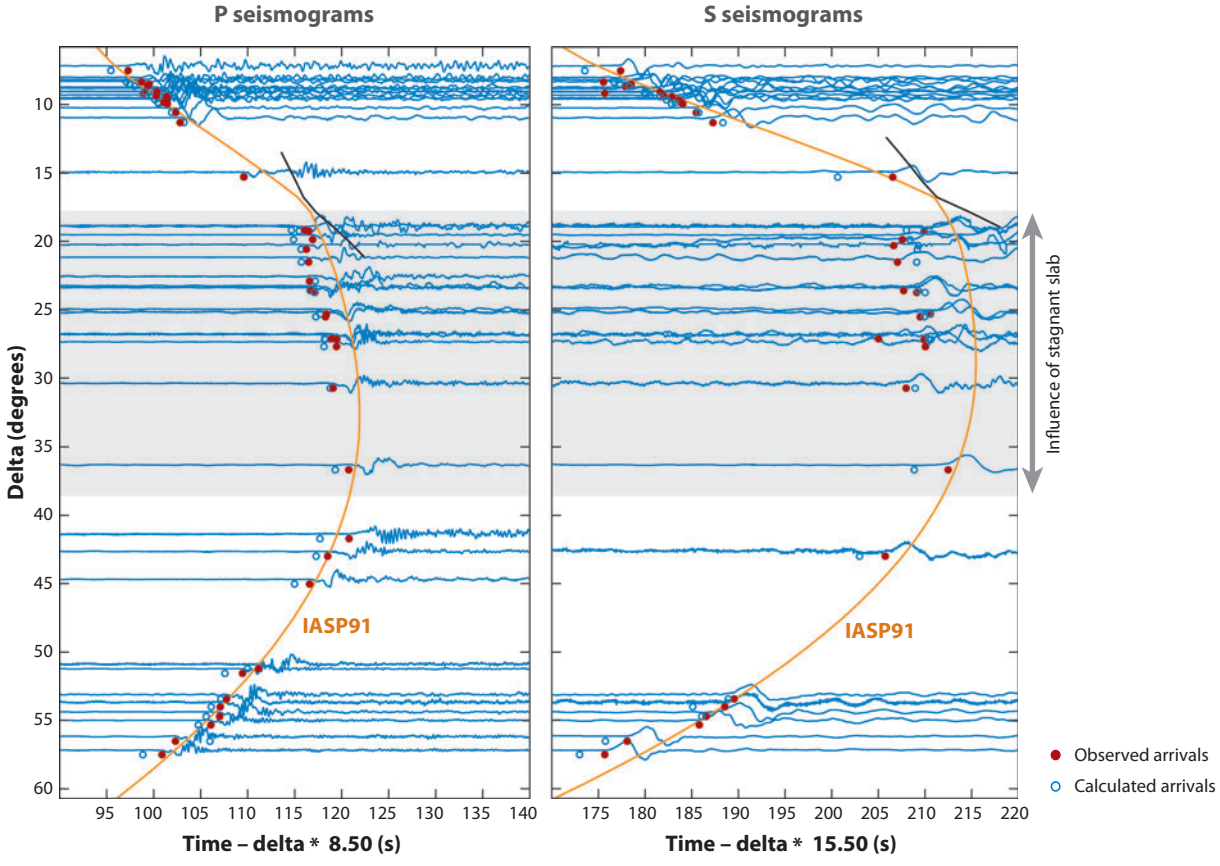


**Figure 4**

Vertical P-wave and transverse S-wave broadband seismograms at stations in southwestern Japan and China for the Izu-Bonin deep shock (h = 494 km) of June 3, 2002 (Sugioka et al. 2007). See **Figure 2*c*** for the hypocenter. The visually identified P-wave and S-wave arrivals are marked by solid dots. The calculated arrivals for the three-dimensional (3D) P and S velocity models are indicated by open dots. The 3D P velocity model is the model of Obayashi et al. (2006), which is converted to the 3D S velocity model using an appropriate conversion factor (see the text for details). The reference travel time curve is IASP91 (Kennett & Engdahl 1991). The gray areas indicate the distance range in which the P- and S-wave propagations should be strongly affected by the stagnant slab.

observed S arrivals in a distance range of our interest. The observed P- and S-wave velocity anomalies and the best-fit value of $R$ can be consistently explained by a lower temperature anomaly of 250–300 K with a PREM Q value, where the $R$ value of $\simeq$1.4 consists of the anharmonicity term of $\simeq$1.1 and the anelasticity term of $\simeq$0.3 (Sugioka et al. 2007). Friederich (2003) used full waveforms of shear and surface waves to show that high shear-velocity subducting slabs along the western Pacific subduction zones are stagnating at the 660 km discontinuity beneath East Asia. Obviously, more studies are needed to characterize stagnant slabs in the northwestern Pacific by S velocity or $Vp/Vs$ ratio.

## THERMAL STATE OF STAGNANT SLAB

The 660 km discontinuity is the boundary between the upper and lower mantle at the nominal depth of 660 km, around which the real boundary plane may undulate.

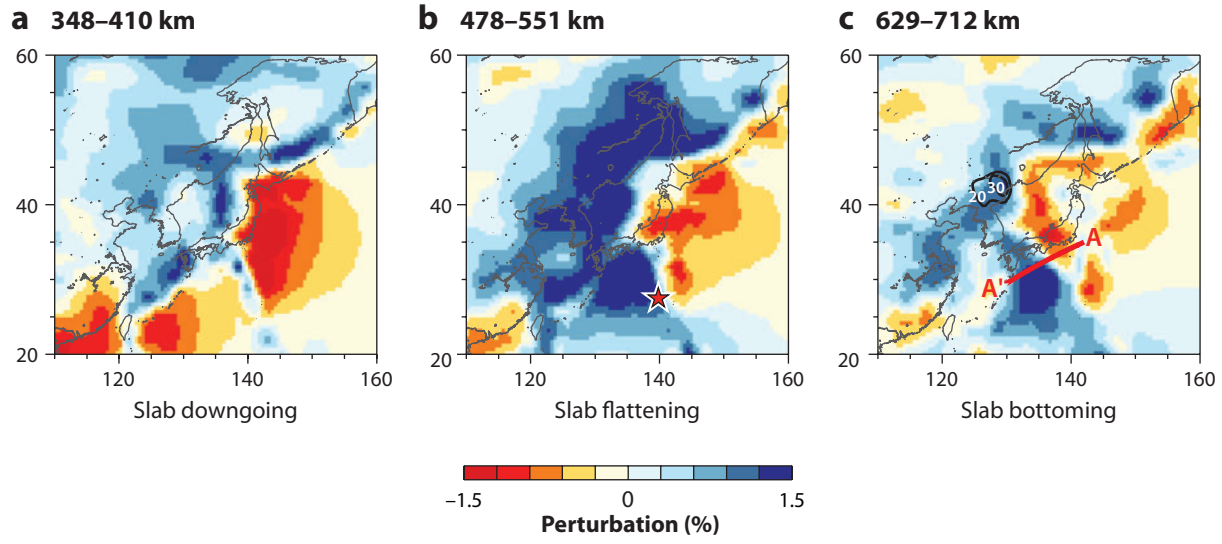


**Figure 5**

P-wave tomographic maps of Obayashi et al. (2006) in three depth ranges: (*a*) just above the 410 km discontinuity, (*b*) in the mid transition zone, and (*c*) around the 660 km discontinuity. Remarkable fast malies in (*a*), (*b*), and (*c*) are associated with the downgoing part, flattening part, and bottoming part of the subducted slab of the Pacific plate, respectively. Line AA′ in (*c*) is the profile along which cross sections are taken in **Figure 6**. The contours in (*c*) are the depth anomalies in kilometers of the 660 km discontinuity obtained by a receiver function analysis of Li & Yuan (2003). The star in (*b*) denotes the epicenter of a deep shock relevant to **Figure 4**.

Some information about how stagnant slab is thermally anomalous comes from studies of the topography of the 660 km discontinuity near the stagnant slab. The global SS (S-wave once bounced at the Earth's surface) precursor study of Flanagan & Shearer (1998) showed that the depression of the 660 km boundary occurs most extensively in the northwestern Pacific, where the depression is ~20 km. They explained this feature by the low temperature effect of horizontally flattened subducting slabs in the mantle transition zone. The simultaneous inversion for the S-velocity distribution and the discontinuity topography by Gu et al. (2003) showed a 660 km depression of the similar magnitude. On the other hand, regional studies using near-source S- to P-converted waves showed a greater slab-induced depression of up to 60 km beneath Izu-Bonin (Wicks & Richards 1993, Castle & Creager 1998). These studies have much higher resolution in the immediate vicinity of the subducting slabs than the global SS precursor studies but little resolution even slightly outside. More recent studies using near-station P- to S-converted waves begin to resolve the apparent discrepancy in the magnitude of the 660 km depression between the global SS-precursor studies and the near-source S- to P-conversion studies.

**Figure 5** shows the tomographic maps in three depth ranges: (*a*) just above the 410 km discontinuity, (*b*) in the mid transition zone, and (*c*) around the 660 km discontinuity (Obayashi et al. 2006). Remarkable fast anomalies in (*a*) are associated with the downgoing part of the Izu-Bonin slab of the Pacific plate. Those in (*b*) spread to horizontal most extensively in the transition zone and correspond to the stagnant part of the subducted slab. Those in (*c*) represent the bottoming part at the intersection of the downgoing and stagnant parts, which can be seen all the way through the southern Kurile, Honshu, and northern Bonin arcs. **Figure 6*a*** explains this situation by taking a tomographic cross section across the Izu-Bonin along profile AA′ in **Figure 5*c***, where the three distinct parts may be identified: the part downgoing through the upper mantle, the part bottoming the 660 km discontinuity, and the part flattening above

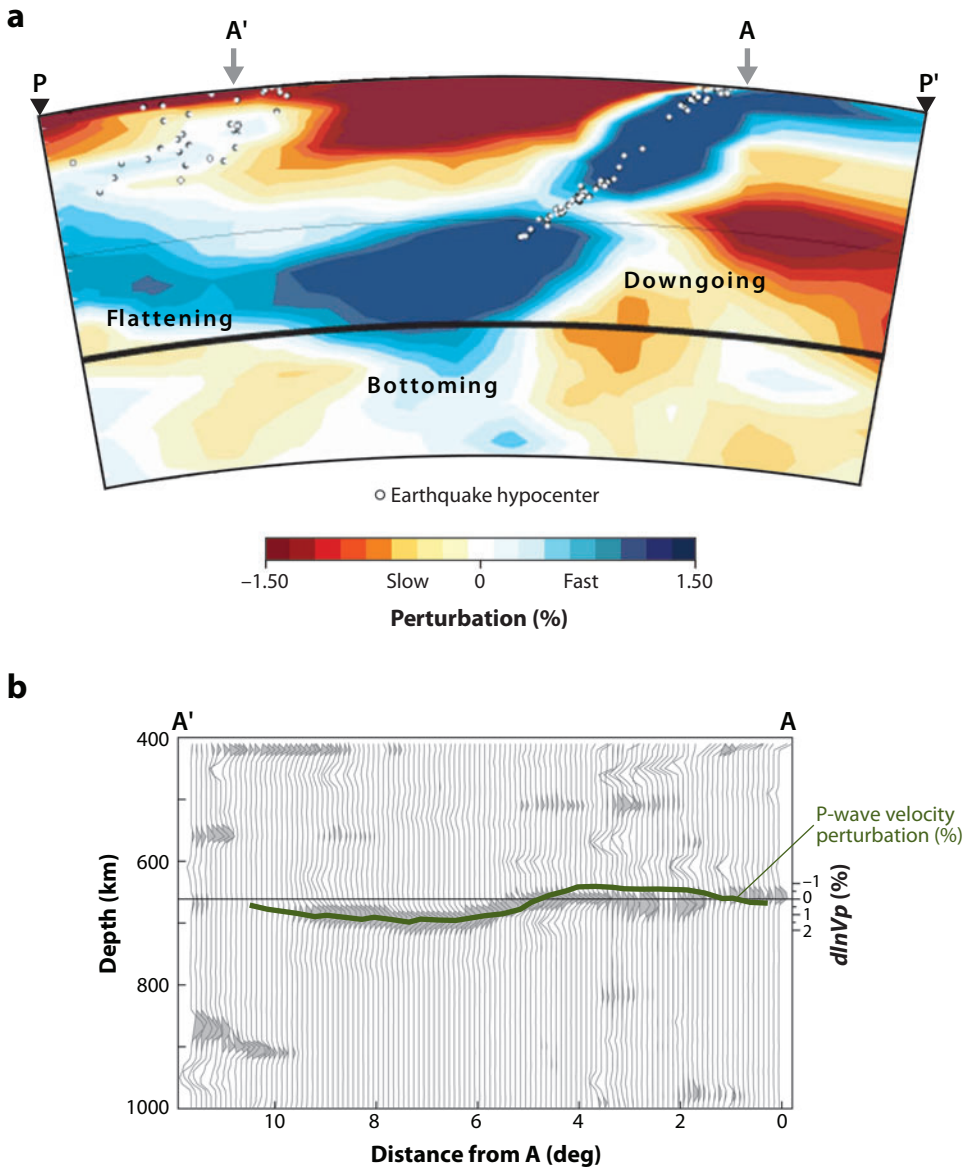


**Figure 6**

Cross sections across the Izu-Bonin arc along profile AA′ in **Figure 5*c***. (*a*) P-wave tomographic cross section of the subducted slab image, showing its downgoing part, bottoming part, and flattening part, which correspond to the slab images in **Figures 5*a***, **5*c*** and **5*b***, respectively (Obayashi et al. 2006). Two arrows A and A′ on the upper frame correspond to A and A′ in the topographic cross section of **Figure 6*b*** and also to A and A′ in the tomographic map of **Figure 5*c***. Triangles P and P′ correspond to P and P′ in the geographic map of **Figure 2**. (*b*) Topographic cross section of the 660 km discontinuity, which is marked by a lateral continuation of a strong signal of P to S conversion (Niu et al. 2005). The depression of the 660 km discontinuity is greatest in the bottoming part of the subducted slab. The P velocity anomaly variation at a constant depth of 660 km along the same profile is superimposed. The topographic depression (*scale on the left*) and the positive velocity anomaly (*scale on the right*) are remarkably parallel to each other.

the 660 km discontinuity, which correspond to the slab images in **Figures 5*a***, **5*c***, and **5*b***, respectively.

**Figure 6*b*** shows the cross section of the topography of the 660 km discontinuity along the same profile AA′, which was obtained by a receiver function analysis of near-station P- to S-converted waves recorded by Hi-Net (a Japanese dense seismic network) (Niu et al. 2005). Depression is greatest in the bottoming part, ∼30 km in agreement with the 20 to 40 km obtained by Li et al. (2000). Depression decreases gradually in the flattened part with increasing distance from the bottoming part. No depression occurs under the obliquely downgoing part. A similar image (the largest depression in the slab's bottoming part and the smaller depression in the flattened part) has also been obtained from a one-station receiver function analysis of P- to S-converted waves for the stagnant slab beneath eastern China, as illustrated in **Figure 5*c*** (Li & Yuan 2003), where the largest depression of a similar magnitude has also been obtained by Li et al. (2000) and Ai et al. (2003). The great depression in the bottoming part and the lesser depression in the flattening part can be qualitatively interpreted in terms of the temperature variation along the 660 km horizon. The 660 km horizon is coldest in the bottoming part of the downgoing slab and is less cold in the horizontal part of the stagnant slab. This temperature variation controls the phase decomposition depth of ringwoodite (a high-pressure phase of the most dominant upper mantle constituent mineral) and the discontinuity depth accordingly. The above results, along with the result of a differential traveltime analysis of the postcursors of the ScS family by Tono et al. (2005), give a consistent interpretation for the apparent difference in the 660 km–discontinuity topography between the global SS-S studies (relatively shallow depression below the slab-flattening part) and the near-source S- to P-conversion studies (relatively deep depression in the slab-bottoming part).

The tomographic and topographic images at the 660 km discontinuity in **Figure 6*a*** and **6*b*** may be compared with each other more quantitatively. In **Figure 6*b***, we superpose the velocity anomaly profile at 660 km depth onto the depth anomaly profile of the 660 km discontinuity. These two anomaly profiles are remarkably parallel to each other, especially in a region of topographic depression, where a fractional P velocity perturbation can be converted to a discontinuity depression using a conversion factor of 20 km/%. This conversion factor may be further converted to a seismological Clapeyron slope, assuming that the 660 km discontinuity is the phase boundary of decomposition of ringwoodite (Levedev et al. 2002).

**Figure 7** shows the result of the recent ultrasonic measurements of P- and S velocities of ringwoodite and majorite at various pressures and temperatures corresponding directly to those in the transition zone (Higo et al. 2007, Irifune et al. 2008), from which we estimate the P velocity of ringwoodite to be $Vp = 10.28$ km/s at a reference state of 21 Ga and 1800 K. The values of $dK/dT$ and $dG/dT$ obtained by Higo et al. (2007), where $K$ and $G$ are bulk and shear moduli, are not significantly different from those obtained by Sinogeikin et al. (2003) and Mayama et al. (2005) using a Brillouin scattering technique and a resonant sphere technique, respectively, at much lower pressures and temperatures. We estimate from **Figure 7** the temperature sensitivity of fractional P velocity perturbation at the reference state to be $(dVp/Vp)/dT = -0.35\%/100$ K. Note a strong nonlinearity of the observed S velocity variation with pressure, which makes $(dVs/Vs)/dT$ and hence $R$ at the reference state larger than those estimated from data in a lower pressure range. This observation may have an important implication for interpreting tomographic images in the transition zone. With the above value of $(dVp/Vp)/dT$, the observed maximum P velocity anomaly of +1.5% in the bottoming part of the subducted slab corresponds to a temperature anomaly of approximately −400 K and the conversion factor of 20 km/% corresponds to a seismological Clapeyron slope of approximately −2.5 MPa/K. Here, we have ignored the anelasticity effect on $(dVp/Vp)/dT$ (Karato 1997) because seismic attenuation is small in the subducting slab, especially for P-waves. The Clapeyron slope of approximately −2.5 MPa/K is not unreasonable for the

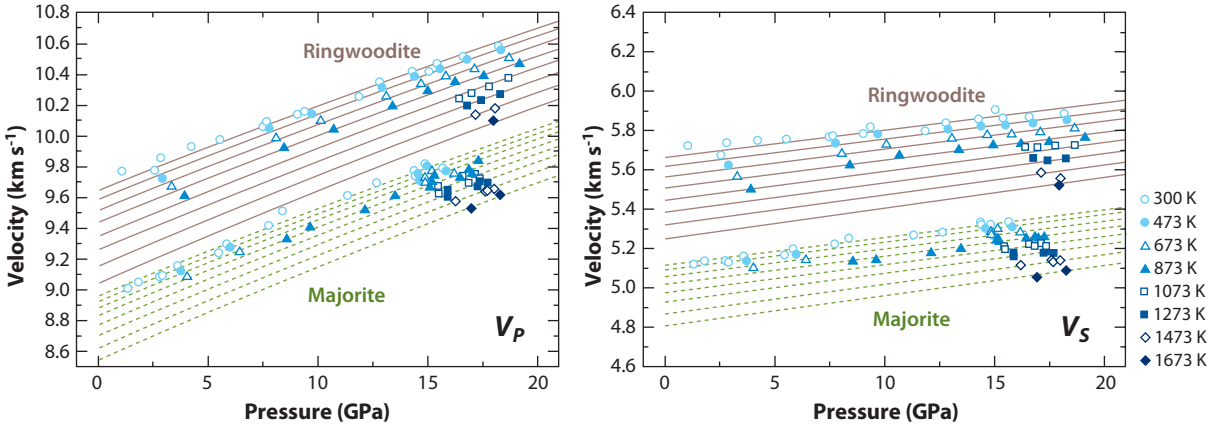


**Figure 7**

P and S velocities of ringwoodite and majorite ultrasonically measured at various pressures and temperatures corresponding directly to those in the transition zone (Higo et al. 2007). The measurements are interpolated theoretically (*lines*). The theoretical interpolations better fit the measured P velocities than the S velocities.

decomposition of ringwoodite, as will be discussed later, and hence lends support to the idea that the 660 km discontinuity is broadly depressed by the low-temperature effect of the stagnant slab and, in turn, that seismic anomalies of the stagnant slab are primarily of thermal origin.

A comparison of the seismic and electrical images of the stagnant slab under southern Europe provides another line of evidence in support of the idea that seismic anomaly of stagnant slab is primarily of thermal origin. **Figure 8** shows the tomographic maps by Schmid et al. (2006), who

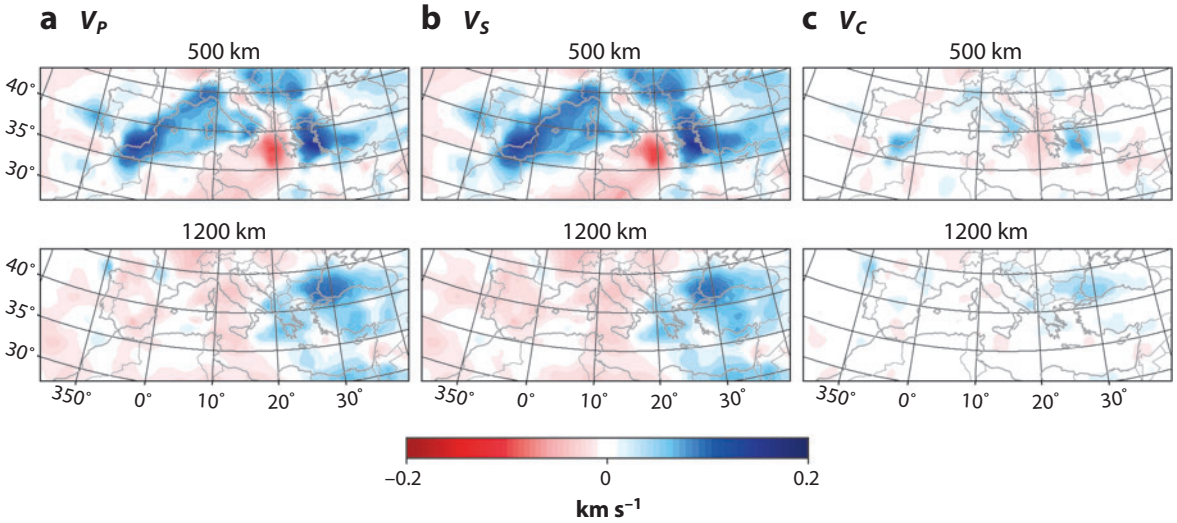


**Figure 8**

Tomographic maps of P, S, and bulk-sound velocity anomalies below southern Europe, obtained by a joint inversion of P and S arrival-time and Rayleigh waveform data [Schmid et al. (2006), with permissions from Elsevier and the authors]. The stagnant slab region is dominated by strong positive anomalies roughly to the west of 20°E in each of the maps at 500 km depth. Roughly to the east of 20°E, the Mediterranean lithosphere appears to subduct to depths beyond 1200 km. Note that the scale is given in km/s and not in %.

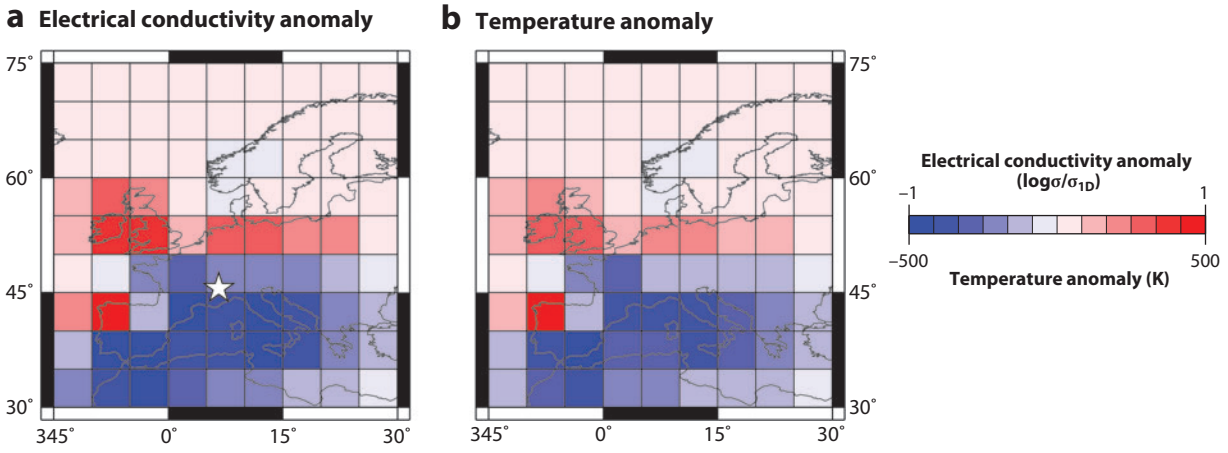


**Figure 9**

(*a*) Tomographic map of electrical conductivity at a depth of 500 km obtained by an inversion of the regional geomagnetic data in Europe (Utada et al. 2005). The map shows the spatial variation of the logarithmic ratio of three-dimensional (3D) electrical conductivity σ to its 1D reference $\sigma_{1D}$. The stagnant slab is imaged as an extensive horizontal spread of low electrical conductivity. The star indicates the location at which Tarits et al. (2004) estimated the underlying electrical conductivity structure. (*b*) Temperature anomaly distribution converted from the electrical conductivity anomaly distribution.

made a joint inversion of P and S arrival-time data and Rayleigh waveform data for the P, S, and bulk-sound velocity structures. Seismic perturbations roughly to the west of 20°E are dominated by the fast anomalies associated with a stagnant slab of the Mediterranean lithosphere in the transition zone. No anomalies are found at depths further below. The fractional P and S velocity changes (*dVp*/*Vp* and *dVs*/*Vs*) in the transition zone are due mainly to this stagnant slab and are 1.5–2.0% and 3–4%, respectively. The value of *R* is then ≃2.0, which is, according to Schmid et al. (2006), consistent with the theoretical estimate of Cammarano et al. (2003). Schmid et al. (2006) argued that the P, S, and bulk-sound velocity anomalies in the transition zone can be consistently explained by the temperatures of the stagnant slab, which are 300–400 K lower than the average.

**Figure 9*a*** shows the tomographic map of electrical conductivity $\log(\sigma/\sigma_{1D})$ at a depth of 500 km based on the regional geomagnetic data in Europe, where σ and $\sigma_{1D}$ are the 3D electrical conductivity and its 1D reference, respectively (Utada et al. 2005). The stagnant slab is imaged as an extensive horizontal spread of low electrical conductivity in a depth range of ∼500 km. This electrical conductivity anomaly distribution is converted to the temperature anomaly distribution using the following relation based on the Arrhenius formulas with activation enthalpy *H*.

$$\frac{dT}{T_{1D}} = \frac{kT_{1D}}{H} \ln \frac{\sigma}{\sigma_{1D}}, \qquad (1)$$

where *k* is Boltzmann's constant and $T_{1D}$ is an assumed temperature of 1750 K at 500 km depth (see Fukao et al. 2004). The experimental value of *H* of ringwoodite is taken from Xu et al. (2000). **Figure 9*b*** shows the temperature anomalies of the stagnant slab estimated with this value, which are on the order of −400 K, in one end of the range (−300 to −400 K) of the estimates from the seismic anomalies by Schmid et al. (2006).

According to Huang et al. (2005), the samples used by Xu et al. (2000), referenced above, contain a small amount of water (∼0.03 Wt%). If the slab below southern Europe contained a larger amount of water than this, the temperature sensitivity of the electrical conductivity of the slab should be higher than the one used here (Wang et al. 2006); accordingly, the temperature

anomalies obtained here may be regarded as an overestimate. This estimate is, however, consistent with the study of Tarits et al. (2004) for the 1D conductivity profile beneath the French Alps (see **Figure 9*a*** for the location). According to this profile, conductivity is anomalously low in the transition zone, where a temperature of 350 to 450 K less than normal is estimated. Tarits et al. (2004) interpreted this result in terms of the subducted slab dehydrated before reaching the transition zone.

## STAGNANT SLAB AND WATER IN THE TRANSITION ZONE

The experimentally determined Clapeyron slope of the postspinel phase change was originally on the order of −3 MPa/K (−2.8 MPa/K, Ito & Takahashi 1989; −3.0 MPa/K, Akaogi & Ito 1993; and −2.9 MPa/K, Irifune et al. 1998). The recent measurements, however, give a more gentle slope, ranging from −2 to −0.5 MPa/K (−2.0 MPa/K, Bina & Helffrich 1994; −0.4 to −2.0 MPa/K, Katsura et al. 2003; and −1.3 MPa/K, Fei et al. 2004). Litasov et al. (2005a,b) determined a Clapeyron slope of −0.5 to −0.8 MPa/K for dry ringwoodite and −2 MPa/K for hydrous ringwoodite. **Figure 10** summarizes their results, where addition of water in ringwoodite makes the Clapeyron slope negatively greater, especially at lower temperatures (Litasov et al. 2006). The "seismological" Clapeyron slope of −2.5 MPa/K estimated from the Izu-Bonin profile in a

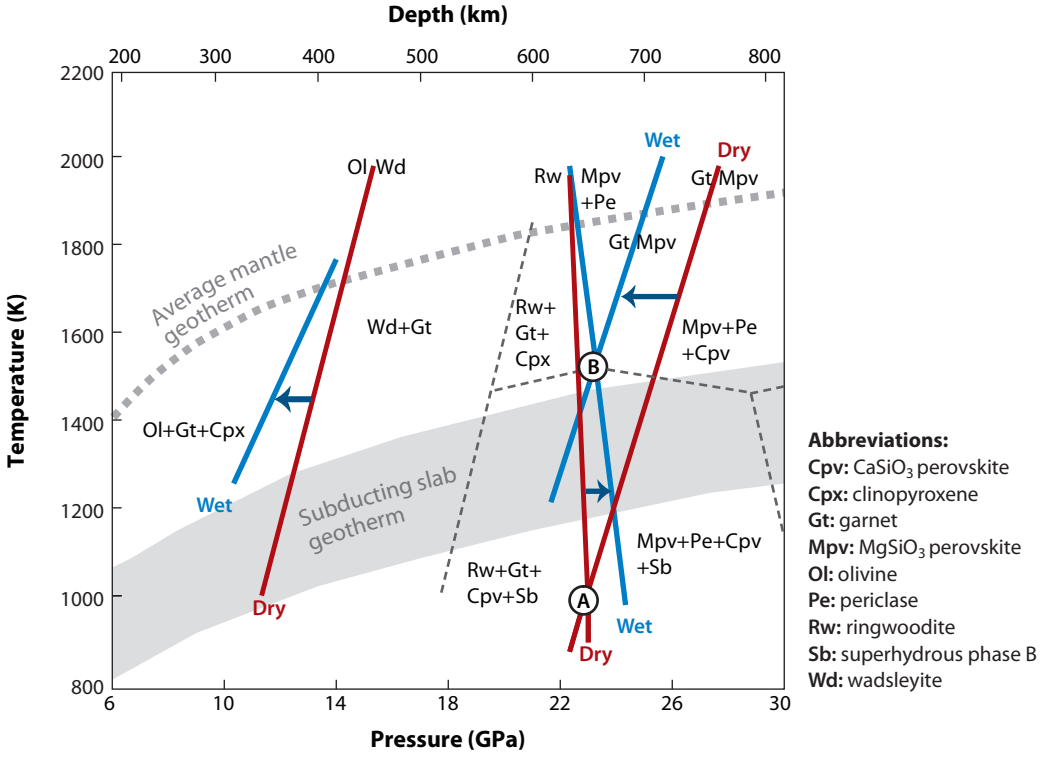


**Figure 10**

Effects of water on the phase transition of olivine at pressures and temperatures corresponding to the 410 km discontinuity and on the phase decomposition of ringwoodite at those corresponding to the 660 km discontinuity (Litasov et al. 2006). Arrows indicate shift of the phase boundary by addition of water. Circled points A and B represent the crossover conditions of decomposition of ringwoodite and post-garnet transition under the dry and wet conditions, respectively.

previous section may imply the presence of water in the slab and the surrounding transition zone, although the issue of experimental determination of the Clapeyron slope of ringwoodite has not yet been settled (Higo et al. 2001).

Water in the transition zone can be stored in wadsleyite and ringwoodite up to 3 Wt% (Inoue et al. 1995, Kohlstedt et al. 1996; see Bolfan-Casanova 2005 for review). Suetsugu et al. (2006) made a simultaneous inversion of the 660 km discontinuity topography and the P velocity perturbations for anomalies in temperature and water content $w$. Using the same dataset as in **Figure 6** and by referring to the $dVp/dT$ value of ringwoodite obtained by Sinogeikin et al. (2003) and the $dVp/dw$ values of ringwoodite obtained by Inoue et al. (1998), Wang et al. (2003) and Jacobsen et al. (2004) [see Jacobsen & Smyth (2006) for more recent results] Suetsugu et al. (2006) showed that with an assumed Clapeyron slope of −2 MPa/K, the bottoming part of the stagnant slab, which apparently overshoots the 660 km depth, is 400–500 K colder than the normal mantle but is not anomalous in water content. Suetsugu et al. (2006) suggested a relative enrichment of water in the transition zone surrounding the stagnant slab rather than in the stagnant slab itself. Such enrichment may occur if water released from the subducting slab is trapped in a thin layer just above the slab and is carried downward with the slab descent, a process suggested by the recent seismological observation of Kawakatsu & Watada (2007). Koyama et al. (2006) examined the results of the seismic and electromagnetic tomography in the northwestern Pacific (Fukao et al. 2004) and estimated a possible water content of ∼0.3 Wt% or more in the transition zone above the stagnant slab beneath the Philippine Sea. Currently, there is little evidence that in the northwestern Pacific the slab in the transition zone is more water-rich than the surrounding (possibly hydrated) transition zone.

Richard et al. (2006) raised an intriguing question: How does water contained in a subducting slab behave when it enters and dwells in the high-solubility transition zone? Water may be expelled from slabs entering the low-solubility lower mantle at 660 km depth, where hydrous ringwoodite and superhydrous phase B decompose (Ohtani et al. 2004, Komabayashi & Omori 2006). Released water may then percolate upward into the transition zone. The transition zone may be hydrated accordingly. In order for this percolation mechanism to be efficient, the released water has to be oversaturated in the high-solubility wadsleyite and ringwoodite. Another way to hydrate the transition zone is from the dehydration of slabs that are stagnating in that zone (Karato et al. 2006). The slab would lose water by diffusive transport, which is complicated by the temperature contrast between the cold slab and the overlying warm mantle. Water diffusion out of the slab and heat diffusion into the slab occur simultaneously and are coupled by the temperature-dependent water solubility. Through this double-diffusive mechanism, according to Richard et al. (2006), essentially 50–100% of the water in the slab is expelled into the transition zone for typical residence times, ∼50 Myr, of slabs floating horizontally across the transition zone. Occurrence of this process over a relatively broad region (the extent of slab deflection) may allow for enhanced distribution of water through the transition zone.

## CONDITIONS FOR SLAB STAGNATION

Stagnant slab has often been discussed in conjunction with the postspinel transition across the 660 km discontinuity (e.g., Fukao et al. 1992). The negative Clapeyron slope of this phase transformation tends to resist straightforward subduction of slabs. Its role has been investigated extensively from the viewpoint of thermal convection since Schubert & Turcotte (1971). Christensen & Yuen (1985) found that the convection pattern changes its mode depending on the Clapeyron slope, from the one-layered mode of convection to the two-layered mode across the intermittent mode. The intermittent mode is characterized by intermittent occurrence of nonstationary one-layered

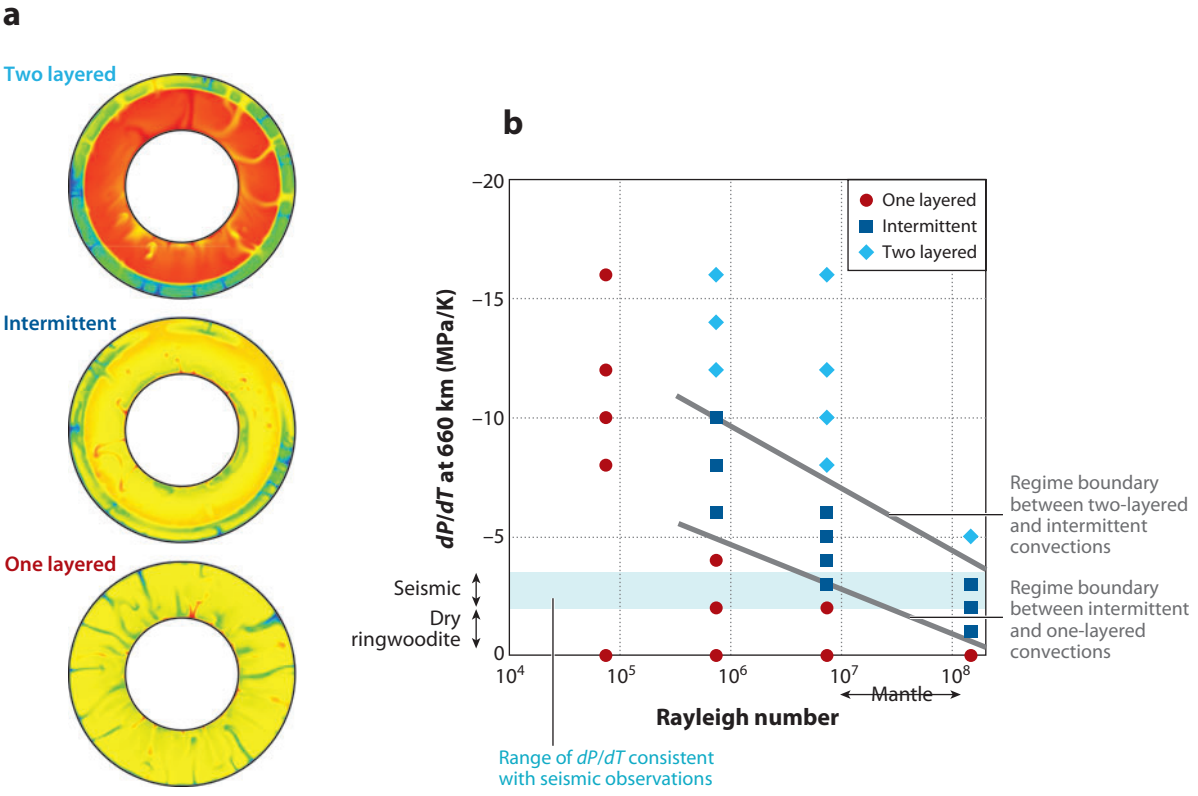


**Figure 11**

Three modes of mantle convection pattern (Yanagisawa et al. 2005). (*a*) Pattern change from the one-layered to the two-layered mode through the intermittent mode. (*b*) Existent ranges of the three modes in the Clapeyron slope versus the Rayleigh number diagram for a uniform-viscosity mantle with three-dimensional (3D) spherical shell geometry. The phase transition occurs at 660 km depth. The Rayleigh number is defined for the system component heated from below. Half of the heating comes from the internally heated system component. The ranges of the "seismological" Clapeyron slope and the basal Rayleigh number for the mantle are shown by arrows along the vertical and horizontal axes, respectively.

(or two-layered) convection during quasistationary two-layered (or one-layered) convection, invoking transient slab stagnation in the transition zone. More realistic convection modeling studies demonstrated that, with plausible values of the Clapeyron slope, the intermittent mode of mantle convection is possible (e.g., Machetel & Weber 1991, Solheim & Peltier 1994). This is also the case with the 3D box and spherical shell geometries (Honda et al. 1993, Tackley et al. 1993, Bunge et al. 1997).

**Figure 11** shows the existent range of the intermittent mode in the *dP/dT* versus *Ra* diagram for a uniform viscosity mantle with 3D spherical shell geometry, where *dP/dT* is the Clapeyron slope at the 660 km discontinuity and *Ra* is the basal Rayleigh number, which is defined for the system component heated from below. Half of the heating comes from the internally heated system component. The basal Rayleigh number covers a wide range up to more than $10^8$, which is the highest value ever achieved for the 3D spherical shell convection modeling (Yanagisawa et al. 2005). The recent experimental values of the Clapeyron slope range from −2 to −0.5 MPa/K for dry ringwoodite and is <−2 MPa/K for wet ringwoodite; the "seismological" Clapeyron slope ranges from −3.5 to −2 MPa/K [e.g., −3.3 MPa/K in Levedev et al. (2002) and −2.5 MPa/K

in the anaysis of **Figure 6** study]. If the basal Rayleigh number of the Earth's mantle ranges from $10^7$ to $10^8$ (e.g., Tackley et al. 1993), and if the transition zone is hydrated as implied by the "seismological" Clapeyron slope, the mantle convection may be in the intermittent mode, although there are many factors that have been ignored in the above discussion.

Such factors include (*a*) one-sided subduction with trench retreat (Christensen 1996), (*b*) temperature- and pressure-dependent viscosity (e.g., Karato & Wu 1993), (*c*) slab-weakening due to grain size reduction after the phase transition (Rubie 1984, Riedel & Karato 1997, Yamazaki et al. 2005, Nishihara et al. 2006), (*d*) olivine metastability in a cold slab (Tetzlaff & Schmeling 2000), (*e*) a viscosity jump across the 660 km discontinuity (Gurnis & Hager 1988, Mitrovica & Forte 1997), (*f*) a thin low-viscosity layer near the 660 km discontinuity (Ito & Sato 1991, Forte et al. 1993), and (*g*) oceanic crust separation near the 660 km discontinuity (van Keken et al. 1996, Karato 1997). Because it is not currently feasible to conduct 3D spherical shell modeling of convection by taking all of these factors into account, 2D numerical fluid simulation with its space restricted near a subduction zone has been attempted extensively (e.g., Čížková et al. 2002, Yoshioka & Sanshadokoro 2002, Tagawa et al. 2007, Torii & Yoshioka 2007).

**Figures 12*a*, 12*b***, and **12*c*** show the effects of the first three factors listed above (Tagawa 2007). One-sided subduction occurs in this model along a megathrust zone with history-dependent



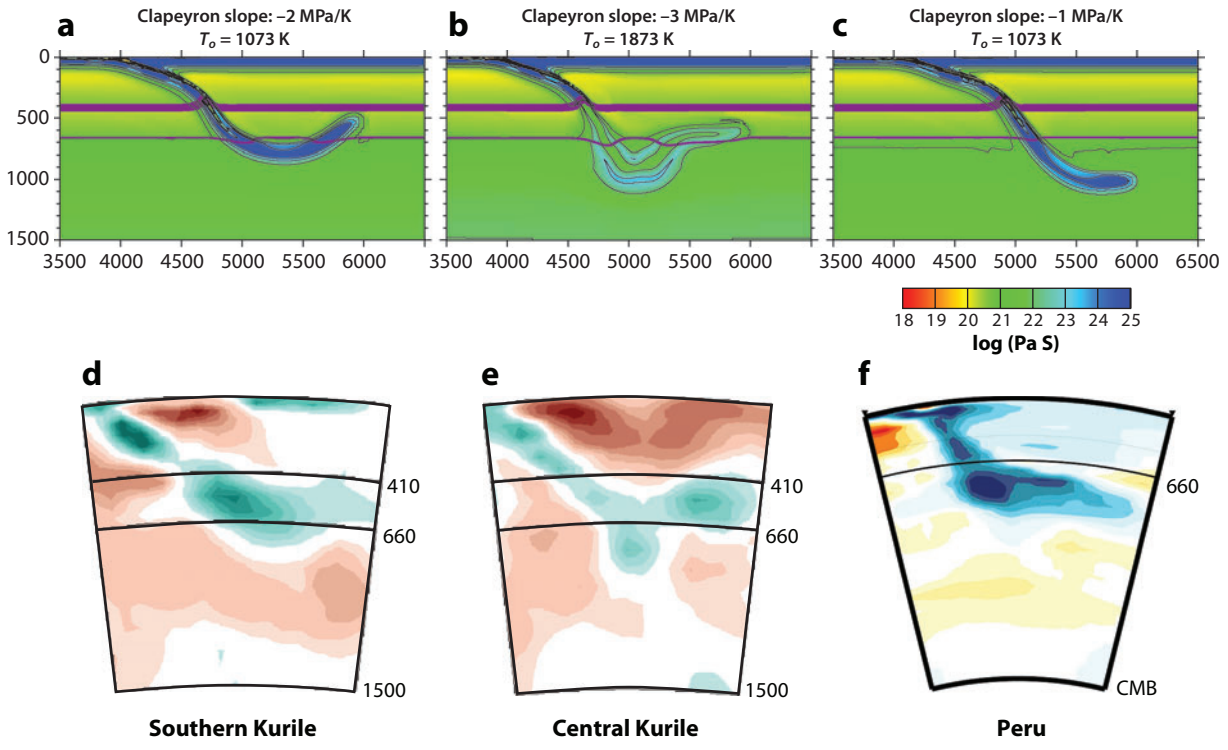


**Figure 12**

Comparison of stagnant slab images between fluid-dynamic simulation and seismic tomography. Fluid-dynamic simulation allows one-sided subduction to occur along the megathrust. Trench migration is also allowed. Viscosity is strongly temperature dependent so that the viscosity profile shown here gives a measure of the temperature profile. Softening due to grain-size reduction associated with phase transition occurs in the colder part ($T < T_o$) of the slab. Clapeyron slope and critical temperature data are from Tagawa (2007). The corresponding P-wave tomographic images of subducted slab are those across the southern and central Kurile arcs (Gorbatov et al. 2000) and that across Peru (Obayashi et al. 2006) and are shown in (*d*), (*e*), and (*f*), respectively.

fault rheology. Trench migration is ensured by letting the side walls of the model-space free in slip. Temperature and pressure dependence of viscosity is from Karato & Wu (1993). Softening due to grain size reduction associated with phase transition is allowed in the colder part ($T < T_o$) of the slab at depths below the 410 km transition. There is no viscosity jump across the 660 km discontinuity. In **Figures 12*a*, 12*b***, and **12*c***, the Clapeyron slope is −2, −3, and −1 MPa/K, and the critical temperature $T_o$ is 1073, 1873, and 1073 K, respectively, although $T_o$ of 1873 K is likely too high to be realistic. The slab is deflected horizontally at depths across the 660 km discontinuity in **Figure 12*a*** and below the 660 km discontinuity in **Figure 12*c***. In **Figure 12*b***, the bottoming part of the downgoing slab sinks into the lower mantle as a blob, leaving the horizontally deflected part above the 660 km discontinuity. Thus, a variety of slab configuration arises without introducing any extra discontinuities at depths below 660 km, as has been already demonstrated by Christensen (1996) and Čížková et al. (2002). For example, Christensen (1996) examined several cases of buckling of a flattened slab with a configuration similar to **Figure 12*b***.

**Figures 12*d***, **12*e***, and **12*f*** show the tomographic images of the subducted slab of the Pacific plate across the southern and central Kurile arcs (Gorbatov et al. 2000) and the subducted slab of the Nazca plate across Peru (Obayashi et al. 2006). The image across the southern Kurile arc (**Figure 12*d***) is very similar to that across the northern Bonin arc (**Figure 3**) and may be compared with the model slab in **Figure 12*a***. The image across central Kurile (**Figure 12*e***) may be compared with the model slab in **Figure 12*b***. The image across Peru may be compared with the model slab in **Figure 12*c***. Although these model slabs are by no means unique, they demonstrate that slab stagnation with varied configuration is a physically feasible process above, across, or below the 660 km discontinuity. The varied configuration can arise from subtle lateral variations in physical properties and the thermomechanical states of the subducting slab and the surrounding mantle.

Stagnant slab has also been identified in the transition zone beneath North America. **Figure 13*a*** shows the tomographic image of the stagnant slab, which is, to the west, detached from the Earth's surface but, to the east, continues down to the mid lower mantle. Schmid et al. (2002) interpreted this slab image in terms of the subduction history of the Farallon plate, as illustrated in **Figure 13*b***. The history involves slab penetration into the lower mantle; slab stagnation above the 660 km discontinuity, with severe internal deformation; and slab detachment from the surface by ridge subduction 30 Ma. Fluid-dynamic simulation by Christensen (1996) suggests that the subducted slab once stagnant above the 660 km discontinuity can sink into the deep lower mantle from its leading edge at a subsequent stage if the Clapeyron slope is large enough and if trench retreat is allowed.

## SLAB FALLING THROUGH THE LOWER MANTLE

Stagnant slab is a temporary feature and is, eventually, likely to fall well into the lower mantle as slab avalanche. A slab avalanche may be responsible for the development of transient intracratonic basins adjacent to convergence zones (Pysklywec & Mitrovica 1998) and the tectonic plate reorganization (Fukao et al. 2001, Pysklywec et al. 2003). Pysklywec & Ishii (2005) made an extensive numerical simulation for the effect of an avalanche of stagnant slabs on subduction dynamics. **Figures 14*b***, **14*c***, and **14*d*** show an example of their results, where the stagnant slab above the 660 km discontinuity is detached with a large gap from the subducting slab at shallow depths. **Figure 14*a*** shows the tomographic image beneath the Bering Sea across the Aleutian arc (Gorbatov et al. 2000). This image is apparently analogous to the model situation at $t = 0$, where the stagnant slab denser than the surrounding mantle is placed above the 660 km discontinuity, across which there is a viscosity jump of a factor of 20 (**Figure 14*b***). Viscous flow coupled with

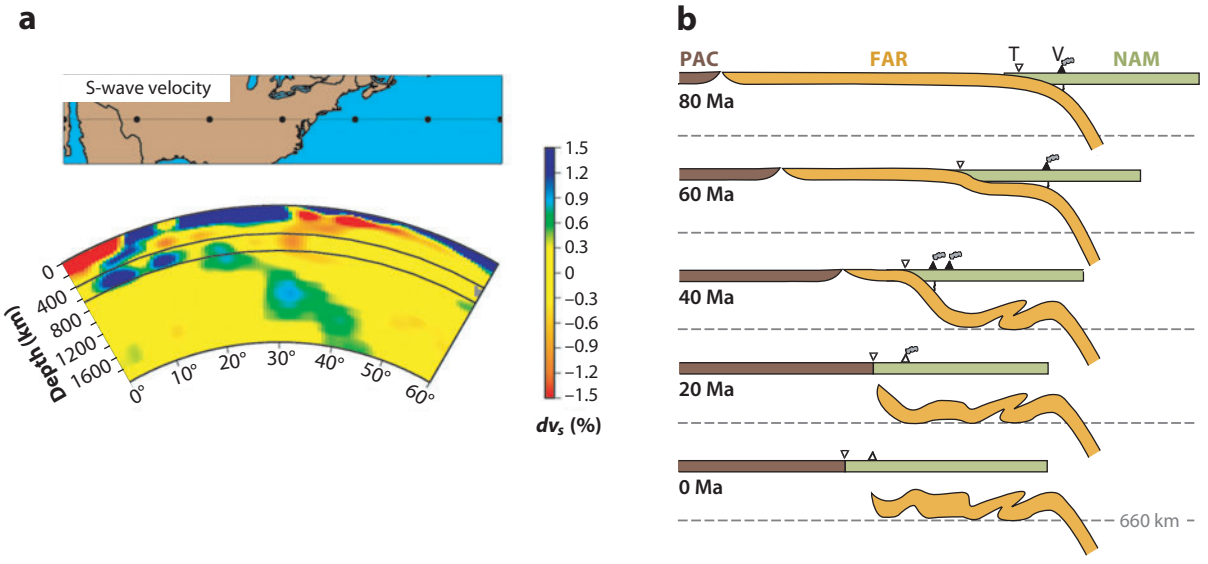


**Figure 13**

S-wave tomographic image of the slab remnant of the Farallon plate beneath North America and its plate tectonic interpretation [figures 3 and 10 in Schmid et al. (2002), with permission from Elsevier]. (*a*) Tomographic cross section is taken along the profile shown at the top, where dots represent the 10° interval of great circle. This image is synthesized from the upper-mantle model of Van der Lee & Nolet (1997) and the whole-mantle model of Grand (1994). The remnant slab of the Farallon plate is now stagnant in the transition zone, which is detached to the west from the Earth's surface but continues to the east down to the mid lower mantle. (*b*) Interpretation of the slab image in terms of the subduction history of the Farallon plate. The history involves slab penetration into the lower mantle, slab stagnation above the 660 km discontinuity, and slab detachment from the surface by ridge subduction. PAC, Pacific plate; FAR, Farallon plate; NAM, North American plate; T, trench; V, volcano. Reproduced from Schmid et al. (2002).

the slab avalanche shifts and deforms the buoyant island arc. It also causes thinning and shearing of the downgoing slab (**Figure 14*c***). Migration of the island arc makes the existing subduction zone inactive and creates a new subduction zone with reversed polarity on the back-arc side (**Figure 14*d***). This simulation implies that avalanche of a stagnant slab can trigger a reorganization of plate motion such as the one that probably occurred at the New Hebrides plate boundary at 10 Ma (Pysklywec et al. 2003). Fukao et al. (2001) argued that a synchronized fall of stagnant slabs along the circum-Pacific might have been a cause for the Eocene plate reorganization (Rona & Richardson 1978, Gordon & Jurdy 1986). Machetel & Humler (2003) attributed the Cretaceous mantle thermal high, which occurred ~125 Ma and had an amplitude of 50 K and a duration of 30 Myr, to an avalache characterized by the advection of cold upper mantle into the lower mantle and the hot return flows from the lower mantle.

If the slab behavior near the 660 km discontinuity is as complex as seen in **Figures 6*a*, 12*d–f*, 13*a***, and **14*a*** and as implied in **Figures 13*b*** and **14*b***, the oceanic crustal part of a slab may configure differently than the rest. It would be difficult, however, to detect such a crustal part within a deeply seated slab by any conventional tomography. Alternatively, reflection analyses of seismic waves from deep shocks have been used to detect seismic reflectors or scatterers at the top of the lower mantle beneath subduction zones, which have been often attributed to fragments of subducted oceanic crust (Kaneshima 2003, Kaneshima & Helffrich 2003, Niu et al. 2003). **Figures 15*a*** and **15*b*** show the results of Niu et al. (2003) and Kaneshima (2003), who plotted their results on the east-west cross sections of the S-wave tomographic image (Widiyantoro et al. 2000)

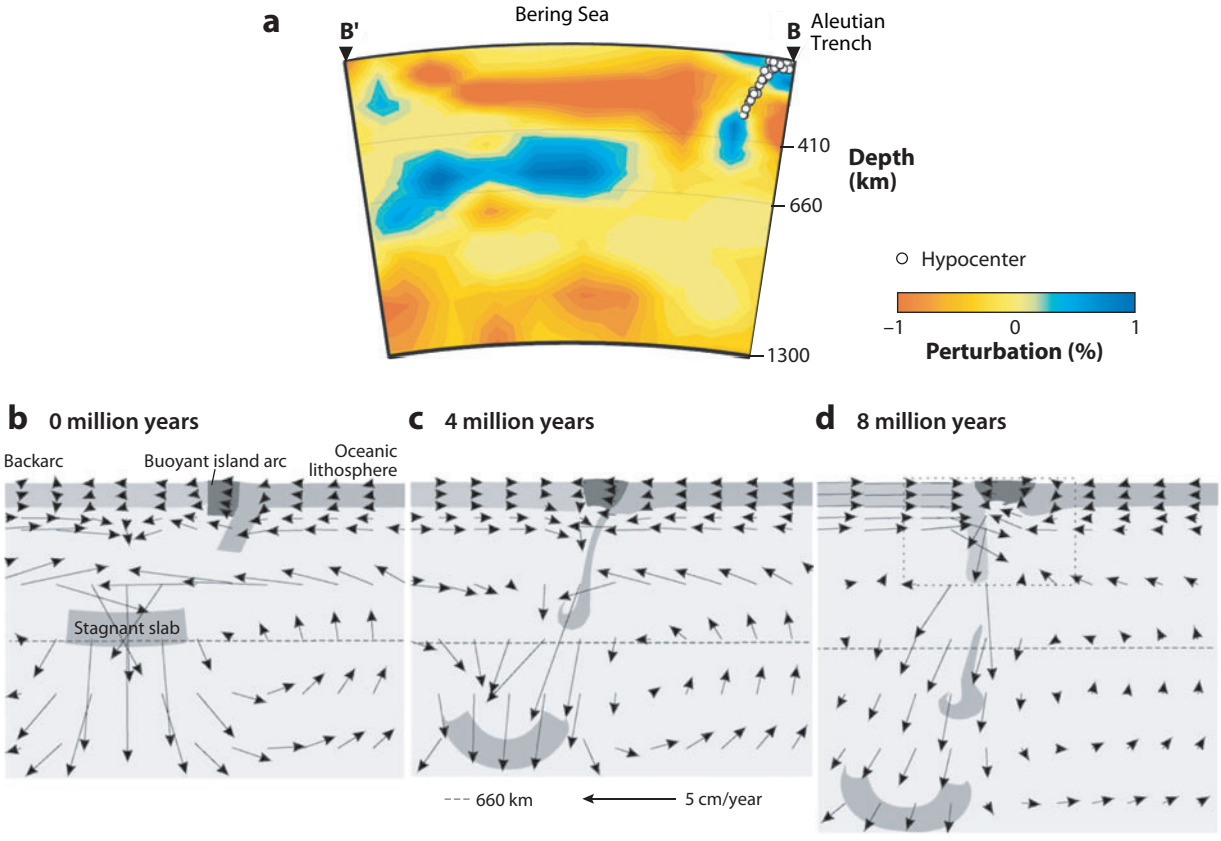


**Figure 14**

(*a*) P-wave tomographic image of the stagnant slab above the 660 km discontinuity, which is well separated from the subducting slab from the Aleutian trench (Gorbatov et al. 2000). (*b–d*) Effect of an avalanche of stagnant slab on subduction dynamics. Reproduced from Pysklywec & Ishii (2005) with permission from Elsevier. A few labels are added. (*b*) The stagnant slab above the 660 km discontinuity is detached, with a large gap from the subducting slab at shallow depths. Across the 660 km discontinuity, there is a viscosity jump of a factor of 20. (*c*) Viscous flow coupled with the slab avalanche shifts and deforms the buoyant island arc. (*d*) Migration of the island arc makes the existing subduction zone inactive and creates a new subduction zone with reversed polarity on the back-arc side.

of the subducted slab across the northern Marian arc and the P-wave tomographic image (Fukao et al. 2001) across the mid Mariana arc, respectively. In **Figure 15*a***, the seismic reflector detected and interpreted as former oceanic crust by Niu et al. (2003) is located at the bottom of the slab in the uppermost lower mantle, where Niu et al. suggested that subducted crust might start sinking separately from the rest of the slab. In **Figure 15*b***, the seismic scatterers detected by Krüger et al. (2001) and Kaneshima (2003) are located within the severely deformed slab indented into the lower mantle. Kaneshima (2003) interpreted these scatterers as fragments of former oceanic crust entrained in the slab upon separation of a crustal component from the stagnant slab near the 660 km discontinuity (van Keken et al. 1996, Karato 1997). The slab images across the Mariana arc in **Figures 15*a*** and **15*b*** may be compared with the model slab in either **Figures 15*c*** or **15*d***, where there is a viscosity increase of a factor of 10 or 30, respectively, across the 660 km discontinuity, which also acts as a phase boundary with a Clapeyron slope of −3 MPa/K (Tagawa 2007). No trench retreat is allowed. In this experiment (Tagawa 2007), the model slab below the 660 km discontinuity is pressed vertically by its indentation into the more viscous lower mantle.

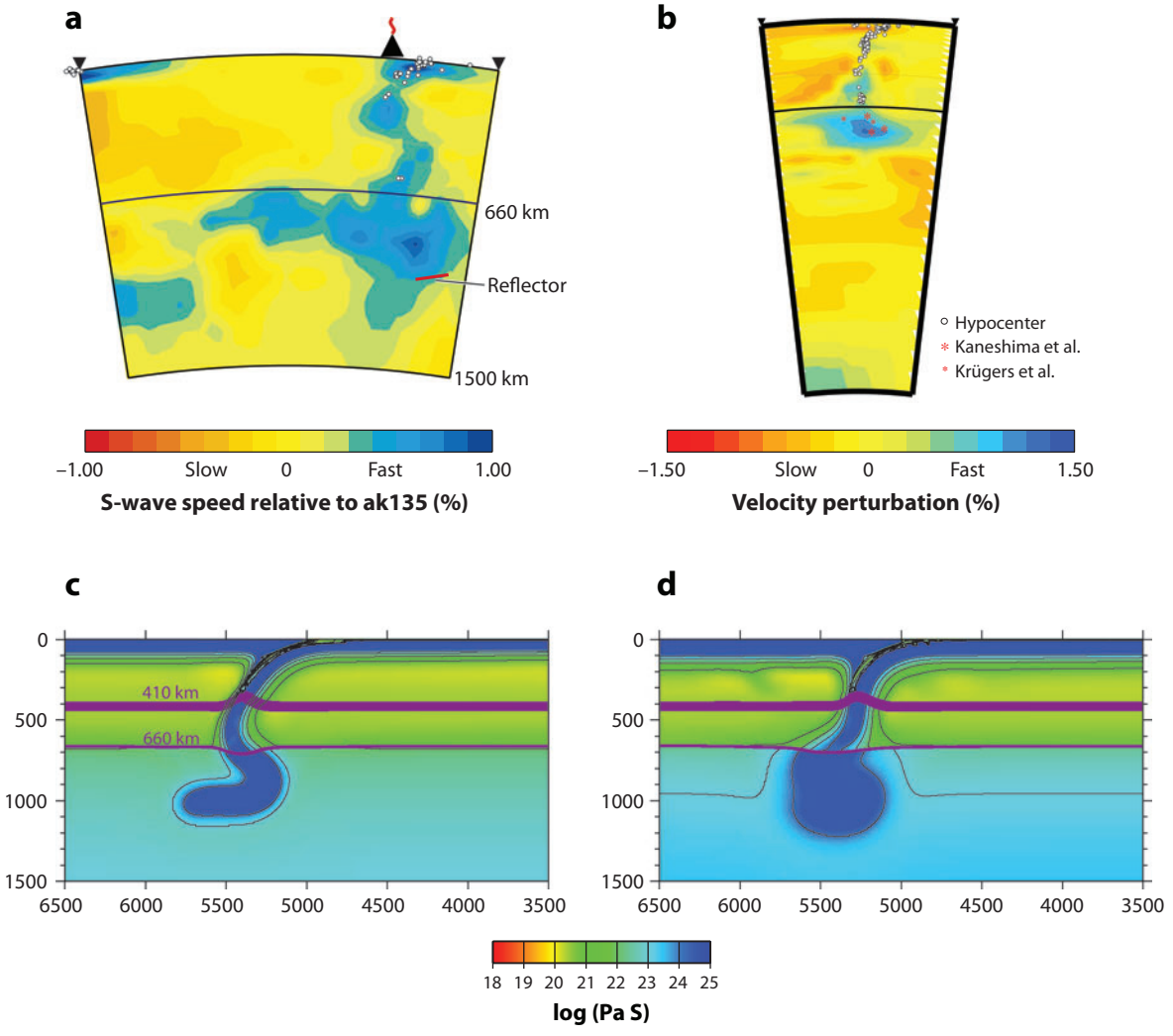


**Figure 15**

(*a*) Seismic reflector (*red line*) detected and superposed by Niu et al. (2003) on the east-west cross section of the S-wave tomographic image (Widiyantoro et al. 2000) of the subducted slab across the northern Marian arc and (*b*) seismic scatterers (small asterisks and large asterisks) detected by Krüger et al. (2001) and Kaneshima (2003) superposed by Kaneshima (2003) on the east-west cross section of the P-wave tomographic image (Fukao et al. 2001) across the mid Mariana arc (color version courtesy of S. Kaneshima). In (*a*), Niu et al. (2003) interpreted the reflector as former oceanic crust. In (*b*), Kaneshima (2003) interpreted the scatterers as fragments of former oceanic crust. (*c*) Simulated subducted slab for a viscosity contrast of a factor of 10 and a Clapeyron slope of −3 MPa/K across the 660 km discontinuity. No trench retreat nor softening due to grain size reduction is allowed (Tagawa 2007). (*d*) Simulated slab for a viscosity contrast of a factor of 30. Other conditions are the same as for (*c*) (Tagawa 2007).

Seismic scatterers interpreted as the fragments of subducted oceanic crust have been reported down to 2000 km (Kaneshima & Helffrich 1999). These deep scatterers are well separated from the stagnant slab images at shallower depths. We note that descent of the oceanic crust could happen even if it is thermally in equilibrium with the surrounding lower mantle because mid-ocean ridge basalt (MORB) crust is known to be denser than the normal lower mantle, as explained below.

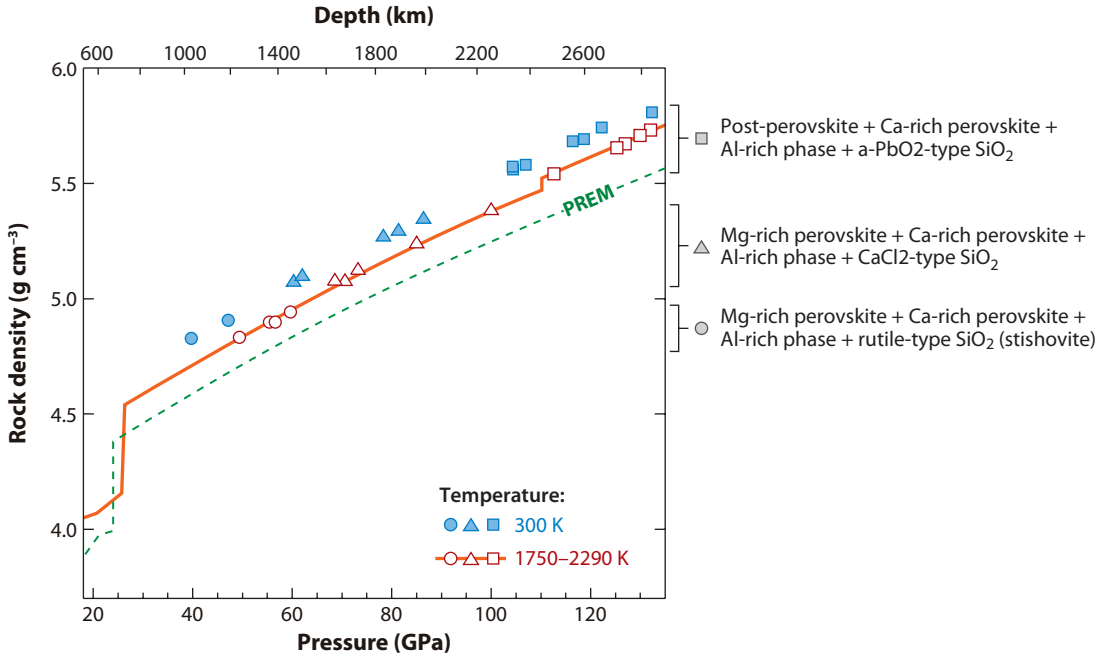


**Figure 16**

Rock density of mid-ocean ridge basalt (MORB) crust in the lower mantle. Modified from Hirose et al. (2005). Dashed line indicates the PREM density. The subducted MORB is denser than the surrounding mantle except between the 660 km boundary and 720 km depth. The density contrast is ~3% at the base of the mantle.

Previous high-pressure studies suggested that MORB crust is buoyant at depths between 660 and 720 km (Irifune & Ringwood 1993, Hirose et al. 1999, Litasov et al. 2004; see **Figure 16**), although the situation may change if the crust is hydrous (Litasov et al. 2006; see **Figure 10**). Hirose et al. (2005) investigated phase relations, mineral chemistry, and density of MORB composition to show that the postperovskite transition (Murakami et al. 2004, Oganov & Ono 2004, Tsuchiya et al. 2004) of MORB composition starts at a pressure lower than the transition pressure for pure $MgSiO_3$ perovskite and ends near that pressure; thus, former MORB crust is denser than the average lower mantle at all depths greater than ~720 km, including the D″ layer. **Figure 16** shows a comparison of the density profile of MORB composition with the reference Earth model PREM (Dziewonski & Anderson 1981) in the entire pressure range of the lower mantle. The density profile along an assumed geotherm indicates that the crustal part of the subducted slab remains denser than the surrounding lower mantle even if it is thermally assimilated to the surrounding lower mantle and thus may eventually accumulate in the D″ layer to differentiate its chemical nature from the rest of the mantle (see also Ono et al. 2001, 2005; Perrillat et al. 2006). Effects of the segregation of subducted oceanic crust on isotopic fractionations in the convecting mantle have been discussed by Christensen & Hofmann (1994), Christensen (2001), Davies (2002), and Brandenburg & van Keken (2007).

Tomographic models show some slab remnants now falling through the lower mantle [see Fukao et al. (2001) for the earlier references on this subject], the most typical examples being those of the Farallon plate and Indian (Tethys) plate. The tomographic maps in the Mediterranean region to the east of 20°E (**Figure 8**; Schmid et al. 2006) show the slab remnant of the Tethyan lithosphere, the descent of which initiated the Late Cretaceous period and now reaches a depth

of at least 1500 km (Faccenna et al. 2003). The seismic signature of this remnant slab in the lower mantle is characterized by a positive P-velocity anomaly, a stronger S-velocity anomaly and a much weaker bulk-sound velocity anomaly. According to Schmid et al. (2006), the value of $R = [dVs/Vs]/[dVp/Vp]$ is ~1.8 in the uppermost 1000 km and appears to increase to ~2.2 below 1200 km. These values of $R$ are in good agreement with those predicted from the mineral physics data, assuming that the anomalies are due solely to temperature perturbation (Trampert et al. 2001, Cammarano et al. 2003). It appears unnecessary to introduce other causes, such as a compositional anomaly, to explain the *Vp*, *Vs*, and bulk-sound velocity anomalies of the remnant slab of the Tethyan lithosphere in the lower mantle.

A slab falling through the lower mantle may eventually reach the core-mantle boundary and accumulate there. It remains uncertain whether the deepest slab images can be interpreted solely by temperature anomalies. In **Figure 1**, the stagnant slab image behind the Bonin trench is underlain by a huge body of seismically fast anomalies at the base of the mantle in the region stretching from the northwestern Pacific to eastern Asia. **Figure 17*a*** (Romanowicz 2003) demonstrates that



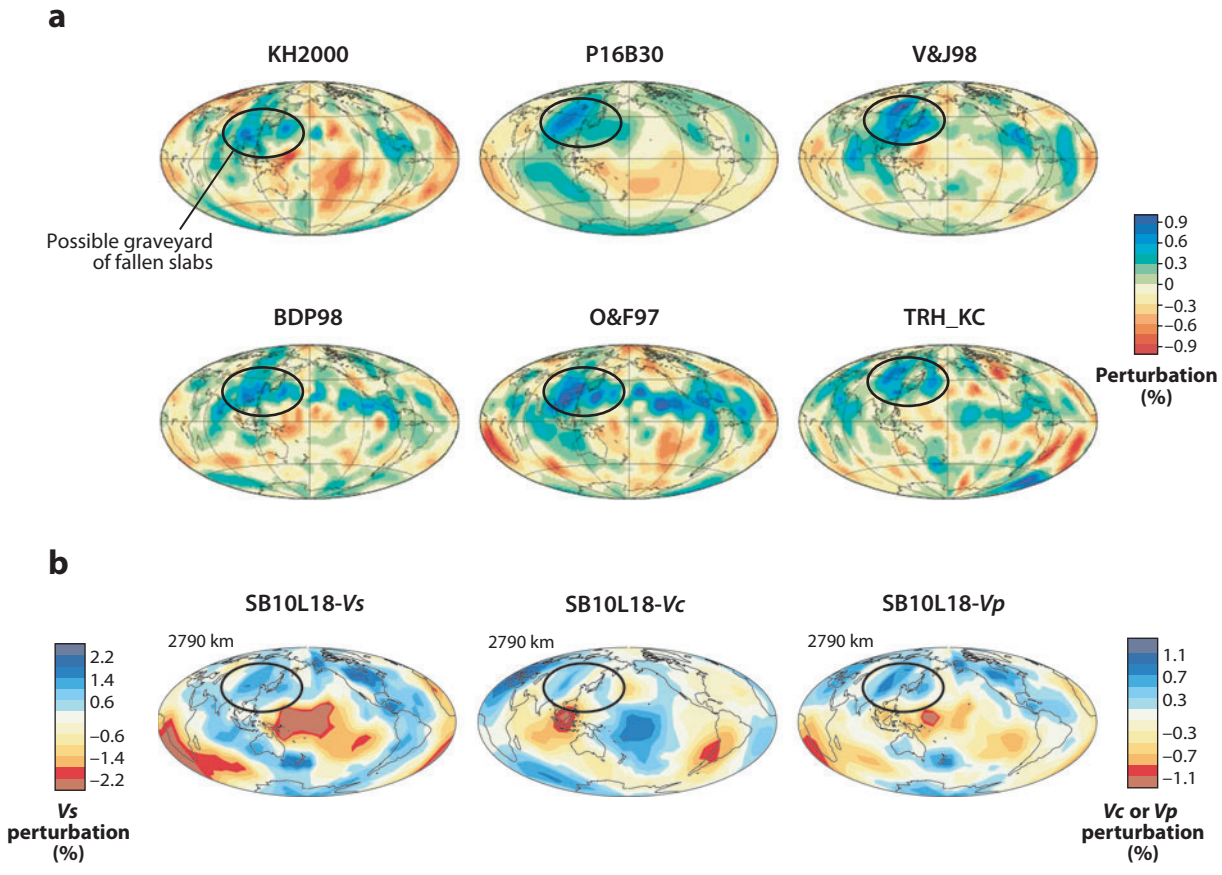


**Figure 17**

(*a*) Lowermost mantle anomalies of global P-wave tomographic models compiled by Romanowicz (2003). (*b*) Perturbation maps of shear velocity, bulk-sound velocity and compressional velocity at the base of the mantle in model SB10L18, by Masters et al. (2000). For all the models, the region encompassing the northwestern Pacific to eastern China is encircled by black ellipses and is commonly characterized by positive velocity anomalies, which may represent an ultimate graveyard of fallen slabs in the northwestern Pacific.

this is the largest body of fast anomalies in the lowermost mantle in almost all of the existing global P-wave tomographic models. This anomalous body develops right under the stagnant slabs of the Pacific plate (**Figure 1**) and may represent an ultimate graveyard of avalanche slabs in the northwestern Pacific. There are no significant fast anomalies at depths between this graveyard image in the lowermost mantle and the stagnant slab image in the transition zone (**Figure 1**), suggesting that most of the avalanche slabs in the northwestern Pacific already reached the core-mantle boundary, whereas the present-day subducting slabs are still accumulating in the transition zone.

In the lowermost mantle near the northwestern end of this anomalous body, Thomas et al. (2004), in a migration study of ScS precursors, detected two seismic discontinuities. The upper discontinuity shows strong topography with a positive impedance contrast, whereas the lower discontinuity exhibits much less topography with a negative impedance contrast. Thomas et al. (2004) interpreted these two discontinuities as the upper and lower surfaces of the cold body of the remnant slab of the ancient Izanagi plate now trapped in the lowermost mantle, although other interpretations may also be possible.

**Figure 17*b*** shows the perturbation maps of shear velocity, bulk-sound velocity and compressional velocity at the base of the mantle in model SB10L18 by Masters et al. (2000). The compressional velocity map again indicates significant positive anomalies in the western Pacific to eastern China, which we have interpreted as the deepest slab remnants. Anomalies in this region are stronger in shear velocity and weaker in bulk-sound velocity than in compressional velocity. Note that the shear velocity and bulk-sound velocity anomalies are positively correlated to each other. Such a positive correlation is in contrast to the anticorrelation observed in the central Pacific (negative shear velocity anomalies versus positive bulk-sound velocity anomalies), where some compositional anomalies have been suggested (Masters et al. 2000). Currently, there is little evidence that the slab remnants in the lowermost mantle under the western Pacific and eastern China are chemically anomalous.

## SUMMARY POINTS

1. Collaboration of seismic and electromagnetic observations, mineral physics measurements, and geodynamic modeling begins to provide a consistent picture of stagnant slab.
2. Stagnant slab is a phenomenon commonly observed beneath subduction zones around the circum Pacific and in the Mediterranean at depths above, across or below the 660 km discontinuity.
3. The "seismological" Clapeyron slope of the 660 km discontinuity is negatively greater than the recent experimental values for decomposition of dry ringwoodite. This observation may suggest that the ringwoodite regime under a subduction zone is hydrated. There is little evidence, however, that the stagnant slab is more water rich than the surrounding (possibly hydrated) transition zone.
4. Numerous fluid-dynamic simulations of plate subduction indicate that stagnant slab with varied configuration is a geodynamically feasible process to occur in some depth range above, across or below the 660 km discontinuity.
5. The heavier crustal component may be detached from a stagnant slab upon its severe distortion to sink separately through the lower mantle.

6. The slab stagnation and the subsequent "avalanche" might have been a cause for plate reorganization events in the geologic past.
7. There is growing evidence suggesting that geophysical signatures, including P, S, and bulk-sound velocities and electrical conductivity, of both stagnant slabs in the transition region and falling slabs in the lower mantle are primarily of thermal origin, compositionally little different from the surrounding mantle.

## DISCLOSURE STATEMENT

The authors are not aware of any biases that might be perceived as affecting the objectivity of this review.

## ACKNOWLEDGMENTS

This research was supported by the Ministry of Education, Culture, Sports, Science, and Technology of Japan through the Deep Slab Project.

## LITERATURE CITED

Ai Y, Zheng T, Xu W, He Y, Dong D. 2003. A complex 660 km discontinuity beneath northeast China. *Earth Planet. Sci. Lett.* 212:63–71

Akaogi M, Ito E. 1993. Refinement of enthalpy measurement of $MgSiO_3$ perovskite and negative pressure-temperature slopes for perovskite-forming reactions. *Geophys. Res. Lett.* 20:1839–42

Bijwaard H, Spakman W, Engdahl ER. 1998. Closing the gap between regional and global travel time tomography. *J. Geophys. Res.* 103:30055–78

Bina CR, Helffrich GR. 1994. Phase transition Clapeyron slopes and transition zone seismic discontinuity topography. *J. Geophys. Res.* 99:15853–60

Bolfan-Casanova N. 2005. Water in the Earth's mantle. *Mineral. Mag.* 69:229–57

Bolton H, Masters G. 2001. Travel times of P and S from the global digital networks: implications for the relative variation of P and S in the mantle. *J. Geophys. Res.* 106:13527–40

Brandenburg JP, van Keken PE. 2007. Deep storage of oceanic crust in a vigorously convecting mantle. *J. Geophys. Res.* 112:B06403

Bunge HP, Richards MA, Baumgardner JR. 1997. A sensitivity study of 3-D spherical mantle convection at $10^8$ Rayleigh number: Effects of depth dependent viscosity, heating mode and an endothermic phase change. *J. Geophys. Res.* 102:11991–2007

Cammarano F, Goes S, Vacher P, Girdini D. 2003. Inferring upper-mantle temperatures from seismic velocities. *Phys. Earth Planet. Inter.* 138:197–222

Castle JC, Creager KC. 1998. Topography of the 660-km discontinuity beneath Izu-Bonin: implications for tectonic history and slab deformation. *J. Geophys. Res.* 103:12511–27

Christensen UR. 1996. The influence of trench migration on slab penetration into the lower mantle. *Earth Planet. Sci. Lett.* 140:27–39

Christensen UR. 2001. Geodynamic models of deep subduction. *Phys. Earth Planet. Inter.* 127:25–34

Christensen UR, Hofmann AW. 1994. Segregation of subducted oceanic crust in the convecting mantle. *J. Geophys. Res.* 99:19867–84

Christensen UR, Yuen DA. 1985. Layered convection induced by phase transitions. *J. Geophys. Res.* 90:291–300

Čížková H, van Hunen J, van den Berg AP, Vlaar NJ. 2002. The influence of rheological weakening and yield stress on the interaction of slabs with the 670 km discontinuity. *Earth Planet. Sci. Lett.* 199:447–57

Davies GF. 2002. Stirring geochemistry in mantle convection models with stiff plates and slabs. *Geochim. Cosmochim. Acta* 66:3125–42

Dziewonski A, Anderson DL. 1981. Preliminary reference Earth model. *Phys. Earth Planet. Inter.* 25:297–356

Faccenna C, Jolivet L, Piromallo C, Morelli A. 2003. Subduction and the depth of convection in the Mediterranean mantle. *J. Geophys. Res.* 108(B2):2099

Fei Y, Van Orman J, Li J, van Westrenen W, Sanloup C, et al. 2004. Experimentally determined postspinel transformation boundary in $Mg_2SiO_4$ using MgO as an internal pressure standard and its geophysical implications. *J. Geophys. Res.* 109:B02305

Flanagan MP, Shearer PM. 1998. Global mapping of topography on transition zone velocity discontinuity by stacking SS precursors. *J. Geophys. Res.* 103:2673–92

Forte AM, Dziewonski AM, Woodward RL. 1993. Aspherical structure of the mantle, tectonic plate motions, nonhydrostatic geoid, and topography of the core-mantle boundary. In *Dynamics of the Earth's Deep Interior and Earth Rotation*, ed. J-L Le Mouel, D Smylie, T Herring, *AGU Geophys. Monogr.* 72, pp. 135–66. Washington, DC: AGU. 189 pp.

Friederich W. 2003. The S-velocity structure of the East Asian mantle from inversion of shear and surface waveforms. *Geophys. J. Int.* 153:88–102

Fukao Y, Koyama T, Obayashi M, Utada H. 2004. Trans-Pacific temperature field in the mantle transition region derived from seismic and electromagnetic tomography. *Earth Planet. Sci. Lett.* 217:425–34

Fukao Y, Obayashi M, Inoue H, Nenbai M. 1992. Subducting slabs stagnant in the mantle transition zone. *J. Geophys. Res.* 97:4809–22

Fukao Y, Widiyantoro S, Obayashi M. 2001. Stagnant slabs in the upper and lower mantle transition region. *Rev. Geophys.* 39:291–323

Gorbatov A, Fukao Y. 2005. Tomographic search for missing link between the remnant Farallon slab and present Cocos subduction. *Geophys. J. Int.* 160:849–54

Gorbatov A, Kennett BLN. 2002. Joint bulk-sound and shear tomography for western Pacific subduction zones. *Earth Planet. Sci. Lett.* 210:527–43

Gorbatov A, Widiyantoro S, Fukao Y, Gordeev E. 2000. Signature of remnant slabs in the North Pacific from P-wave tomography. *Geophys. J. Int.* 142:27–36

Gordon RG, Jurdy DM. 1986. Cenozoic global plate motions. *J. Geophys. Res.* 91:12389–406

Grand SP. 1994. Mantle shear structure beneath the Americas and surrounding oceans. *J. Geophys. Res.* 99:11591–621

Grand SP. 2002. Mantle shear-wave tomography and the fate of subducted slabs. *Philos. Trans. R. Soc. London Ser. A* 360:2475–91

Grand SP, van der Hilst R, Widiyantoro S. 1997. Global seismic tomography: a snapshot of convection in the Earth. *GSA Today* 7:1–7

Gu YJ, Dziewonski A, Ekstrom G. 2003. Simultaneous inversion for mantle shear velocity and topography of transition discontinuities. *Geophys. J. Int.* 154:559–83

Gurnis M, Hager BH. 1988. Controls on the structure of subducted slabs. *Nature* 335:317–22

Hafkenscheid E, Wortel MJR, Spakman W. 2006. Subduction history of the Tethyan region derived from seismic tomography and tectonic reconstructions. *J. Geophys. Res.* 111:B08401

Higo Y, Inoue T, Irifune T. 2001. Effect of water on the spinel-postspinel transformation in $Mg_2SiO_4$. *Geophys. Res. Lett.* 28:3505–8

Higo Y, Inoue T, Irifune T, Funakoshi K-i, Li B. 2007. Elastic wave velocities of $(Mg_{0.91}\ Fe_{0.09})_2SiO_4$ ringwoodite under P-T conditions of the mantle transition region. *Phys. Earth Planet. Inter.* 166:167–74

Hirose K, Fei Y, Ma Y, Mao HK. 1999. The fate of subducted basaltic crust in the Earth's lower mantle. *Nature* 397:53–56

Hirose K, Takafuji N, Sata N, Ohishi Y. 2005. Phase transition and density of subducted MORB crust in the lower mantle. *Earth Planet. Sci. Lett.* 237:239–51

Honda S, Yuen DA, Balachandar S, Reuteler D. 1993. Three-dimensional instabilities of mantle convection with multiple phase transitions. *Science* 259:1308–11

Huang J, Zhao D. 2006. High-resolution mantle tomography of China and surrounding regions. *J. Geophys. Res.* 111:B09305

Huang X, Yousheng X, Karato S. 2005. Water content in the transition zone from electrical conductivity of wadsleyite and ringwoodite. *Nature* 434:746–49

Ichiki M, Baba K, Obayashi M, Utada H. 2006. Water content and geotherm in the upper mantle above the stagnant slab: Interpretation of electrical conductivity and seismic P-wave velocity models. *Phys. Earth Planet. Inter.* 155:1–15

Inoue T, Weidner DJ, Northrup PA, Parise JB. 1998. Elastic properties of hydrous ringwoodite (γ-phase) on $Mg_2SiO_4$. *Earth Planet. Sci. Lett.* 160:107–13

Inoue T, Yurimoto H, Kudoh Y. 1995. Hydrous modified spinel, $Mg_{1.75}SiH_{0.5}O_4$: a new water reservoir in the mantle transition region. *Geophys. Res. Lett.* 22:117–20

Irifune T, Higo Y, Inoue T, Kono Y, Funakoshi K. 2008. Sound velocities of majorite garnet and the composition of the mantle transition region. *Nature* 451:814–17

Irifune T, Nishiyama N, Kuroda K, Inoue T, Isshiki M, et al. 1998. The postspinel phase boundary in $Mg_2SiO_4$ determined by in situ X-ray diffraction. *Science* 279:1698–700

Irifune T, Ringwood AE. 1993. Phase transformations in subducted oceanic crust and buoyancy relationships at depths of 600–800 km in the mantle. *Earth Planet. Sci. Lett.* 117:101–10

Ito E, Sato H. 1991. Aseismicity in the lower mantle by superplasticity of the descending slab. *Nature* 351:140–41

Ito E, Takahashi E. 1989. Post-spinel transformation in the system $Mg_2SiO_4$-$Fe_2SiO_4$ and some geophysical implications. *J. Geophys. Res.* 94:10637–46

Jacobsen SD, Smyth JR. 2006. Effect of water on the sound velocities of ringwoodite in the transition zone. See Jacobsen & van der Lee 2006, pp. 131–45

Jacobsen SD, Smyth JR, Spetzler H, Holl CM, Frost DJ. 2004. Sound velocity and elastic constants of iron-bearing hydrous ringwoodite. *Phys. Earth Planet. Inter.* 143/144:47–56

Jacobsen SD, van der Lee S, eds. 2006. *Earth's Deep Water Cycle. AGU Geophys. Monogr.* 168. Washington, DC: AGU. 313 pp.

Kaneshima S. 2003. Small-scale heterogeneity at the top of the lower mantle around the Mariana slab. *Earth Planet. Sci. Lett.* 209:85–101

Kaneshima S, Helffrich G. 1999. Dipping low-velocity layer in the midlower mantle: evidence for geochemical heterogeneity. *Science* 283:1888–91

Kaneshima S, Helffrich G. 2003. Subparallel dipping heterogeneities in the mid-lower mantle. *J. Geophys. Res.* 108(B5):2272

Karato S. 1997. On the separation of crustal component from subducted oceanic lithosphere near the 660 km discontinuity. *Phys. Earth Planet. Inter.* 99:103–11

Karato S, Bercovici D, Leathy G, Richard G, Jing Z. 2006. The transition-zone water filter model for global material circulation: Where do we stand? See Jacobsen & van der Lee 2006, pp. 289–313

Karato S, Wu P. 1993. Rheology of the upper mantle: a synthesis. *Science* 260:771–78

Katsura T, Yamada H, Shinmei T, Kubo A, Ono S, et al. 2003. Post-spinel transition in $Mg_2SiO_4$ determined by high P-T in situ X-ray diffractometry. *Phys. Earth Planet. Inter.* 136:11–24

Kawakatsu H, Watada S. 2007. Seismic evidence for deep water transportation in the mantle. *Science* 316:1468–71

Kennett BLN, Engdahl E. 1991. Traveltimes for global earthquake location and phase identification. *Geophys. J. Int.* 105:429–65

Kennett BLN, Gorbatov A. 2004. Seismic heterogeneity in the mantle—strong shear wave signature of slabs from joint tomography. *Phys. Earth Planet. Inter.* 146:87–100

Kohlstedt DL, Keppler H, Rubie DC. 1996. Solubility of water in the α, β, and γ phases of $(Mg, Fe)_2SiO_4$. *Contrib. Mineral. Pet.* 123:345–57

Komabayashi T, Omori S. 2006. Internally consistent thermodynamic data set for dense hydrous magnesium silicate up to 35 GPa, 1600°C: Implications for water circulation in the Earth's deep mantle. *Phys. Earth Planet. Inter.* 156:89–107

Koyama T, Shimizu H, Utada H, Ichiki M, Ohtani E, Hae R. 2006. Water content in the mantle transition zone beneath the North Pacific derived from the electrical conductivity anomaly. See Jacobsen & van der Lee 2006, pp. 237–49

Krüger F, Baumann M, Scherbaum F, Weber M. 2001. Mid mantle scatterers near the Mariana slab detected with a double array method. *Geophys. Res. Lett.* 28:667–70

Lei J, Zhao D. 2005. P-wave tomography and origin of the Changbai intraplate volcano in Northeast Asia. *Tectonophysics* 397:281–95

Lei J, Zhao D. 2006. Global P-wave tomography: on the effect of various mantle and core phases. *Phys. Earth Planet. Inter.* 154:44–69

Levedev S, Chevrot S, van der Hilst RD. 2002. Seismic evidence for olivine phase changes at the 410- and 660-kilometer discontinuities. *Science* 296:1300–2

Li X, Sobolev SV, Kind R, Yuan X, Estabrook CH. 2000. A detailed receiver function image of the upper mantle discontinuity in the Japan subduction zone. *Earth Planet. Sci. Lett.* 183:527–41

Li X, Yuan X. 2003. Receiver functions in northeast China—implications for slab penetration into the lower mantle in northwest Pacific subduction zone. *Earth Planet. Sci. Lett.* 216:679–91

Li XD, Romanowicz B. 1996. Global mantle shear velocity model using nonlinear asymptotic coupling theory. *J. Geophys. Res.* 101:22245–72

Litasov KD, Ohtani E, Sano A. 2006. Influence of water on major phase transitions in the Earth's mantle. See Jacobsen & van der Lee 2006, pp. 95–111

Litasov KD, Ohtani E, Sano A, Suzuki A. 2005a. Wet subduction versus cold subduction. *Geophys. Res. Lett.* 32:L13312

Litasov KD, Ohtani E, Sano A, Suzuki A, Funakoshi K. 2005b. In situ X-ray diffraction study of postspinel transformation in a peridotite mantle: implication for the 660-km discontinuity. *Earth Planet. Sci. Lett.* 238:311–28

Litasov KD, Ohtani E, Suzuki A, Kawazoe T, Funakoshi K. 2004. Absence of density crossover between basalt and peridotite in the cold slabs passing through 660 km discontinuity. *Geophys. Res. Lett.* 31(24):L24607

Machetel P, Humler E. 2003. High mantle temperature during Cretaceous avalanche. *Eart Planet. Sci. Lett.* 208:125–33

Machetel P, Weber P. 1991. Intermittent layered convection in a model mantle with an endothermic phase change at 670 km. *Nature* 350:55–57

Marone F, van der Lee S, Giardini D. 2004. Three-dimensional upper-mantle S-velocity model for the Eurasia-Africa plate boundary region. *Geophys. J. Int.* 158:109–30

Masters G, Laske G, Bolton H, Dziewonski A. 2000. The relative behavior of shear velocity, bulk sound speed, and compressional velocity in the mantle: implications for chemical and thermal structure. In *Earth's Deep Interior*, ed. S Karato, *AGU Geophys. Monogr.* 117, pp. 63–87. Washington, DC: 289 pp.

Mayama M, Suzuki I, Saito T, Ohno I, Katsura T, Yoneda A. 2005. Temperature dependence of the elastic moduli of ringwoodite. *Phys. Earth Planet. Inter.* 148:353–59

Mitrovica JX, Forte AM. 1997. Radial profile of mantle viscosity: results from the joint inversion of convection and postglacial rebound observables. *J. Geophys. Res.* 102:2751–70

Murakami M, Hirose K, Kawamura K, Sata N, Ohishi Y. 2004. Post-perovskite phase transition in $MgSiO_3$. *Science* 304:855–58

Nishihara Y, Shinmei T, Karato S. 2006. Grain-growth kinetics in wadsleyite: Effects of chemical environment. *Phys. Earth Planet. Inter.* 154:30–43

Niu F, Kwakatsu H, Fukao Y. 2003. Seismic evidence for a chemical heterogeneity in the midmantle: A slightly dipping and strong seismic reflector at mid-depth beneath the Mariana subduction zone. *J. Geophys. Res.* 108(B9):2419

Niu F, Levander A, Ham S, Obayashi M. 2005. Mapping the subducting Pacific slab beneath southwest Japan with Hi-net receiver functions. *Earth Planet. Sci. Lett.* 239:9–17

Obayashi M, Sugioka H, Yoshimitsu J, Fukao Y. 2006. High temperature anomalies oceanward of subducting slabs at the 410-km discontinuity. *Earth Planet. Sci. Lett.* 243:149–58

Oganov AR, Ono S. 2004. Theoretical and experimental evidence for a postperovskite phase of $MgSiO_3$ in Earth's D″ layer. *Nature* 430:445–48

Ohtani E, Litasov K, Hosoya T, Kubo T, Kondo T. 2004. Water transport into the deep mantle and formation of a hydrous transition zone. *Phys. Earth Planet. Inter.* 143/144:255–69

Okino K, Ando M, Kaneshima S, Hirahara K. 1989. The horizontally lying slab. *Geophys. Res. Lett.* 16:1059–2062

Ono S, Ito E, Katsura T. 2001. Mineralogy of subducted basaltic crust (MORB) from 25 to 37 GPa, and chemical heterogeneity of the lower mantle. *Earth Planet. Sci. Lett.* 190:57–63

Ono S, Ohishi Y, Isshiki M, Watanuki T. 2005. In situ X-ray observations of phase assemblages in peridotite and basalt compositions at lower mantle conditions: implications for density of subducted oceanic plate. *J. Geophys. Res.* 110:BO2208

Perrillat J-P, Ricolleau A, Daniel I, Fiquet G, Mezouar M, et al. 2006. Phase transformations of subducted basaltic crust in the upmost lower mantle. *Phys. Earth Planet. Inter.* 157:139–49

Piromallo C, Morelli A. 2003. P wave tomography of the mantle under the Alpine-Mediterranean area. *J. Geophys. Res.* 108(B2)2065

Pysklywec RN, Ishii M. 2005. Time dependent subduction dynamics driven by the instability of stagnant slabs in the transition zone. *Phys. Earth Planet. Inter.* 149:115–32

Pysklywec RN, Mitrovica JX. 1998. Mantle flow mechanisms for the large-scale subsidence of continental interiors. *Geology* 26:687–90

Pysklywec RN, Mitrovica JX, Ishii M. 2003. Mantle avalanche as a driving force for tectonic reorganization in the southwest Pacific. *Earth Planet. Sci. Lett.* 209:29–38

Replumaz A, Kárason H, van der Hilst RD, Besse J, Tapponnier P. 2004. 4-D evolution of SE Asia's mantle from geological reconstructions and seismic tomography. *Earth Planet. Sci. Lett.* 221:103–15

Richard G, Bercovici D, Karato S. 2006. Slab dehydration in the Earth's mantle transition zone. *Earth Planet. Sci. Lett.* 251:156–67

Riedel MR, Karato S. 1997. Grain-size evolution in subducted oceanic lithosphere associated with the olivine-spinel transformation and its effects on rheology. *Earth Planet. Sci. Lett.* 148:27–43

Romanowicz B. 2003. Global mantle tomography: progress status in the past 10 years. *Annu. Rev. Earth Planet. Sci.* 31:303–28

Rona PA, Richardson ES. 1978. Early Cenozoic global plate reorganization. *Earth Planet. Sci. Lett.* 40:1–11

Rubie DC. 1984. The olivine-spinel transformation and the rheology of subducting lithosphere. *Nature* 308:505–8

Schmid C, Goes S, van der Lee S, Giardini D. 2002. Fate of the Cenozoic Farallon slab from a comparison of kinematic thermal modeling with tomographic images. *Earth Planet. Sci. Lett.* 204:17–32

Schmid C, van der Lee S, Giardini D. 2006. Correlated shear and bulk moduli to 1400 km beneath the Mediterranean region. *Phys. Earth Planet. Inter.* 159:213–24

Schubert G, Turcotte GL. 1971. Phase changes and mantle convection. *J. Geophys. Res.* 76:1424–32

Sinogeikin SV, Bass JD, Katsura T. 2003. Single-crystal elasticity of ringwoodite to high pressures and high temperatures: implications for 520 km seismic discontinuity. *Phys. Earth Planet. Inter.* 136:41–66

Solheim LP, Peltier WP. 1994. Avalanche effects in phase transition modulated thermal convection: a model of Earth's mantle. *J. Geophys. Res.* 99:6997–7018

Su W, Woodward RL, Dziewonski AM. 1994. Degree 12 model of shear velocity heterogeneity in the mantle. *J. Geophys. Res.* 99:6945–80

Suetsugu D, Inoue T, Yamada A, Zhao D, Obayashi M. 2006. Towards mapping the three-dimensional distribution of water in the transition zone from P-velocity tomography and 660-km discontinuity depths. See Jacobsen & van der Lee 2006, pp. 237–49

Sugioka H, Suetsugu D, Obayashi M, Fukao Y, Gao Y. 2007. Body wave travel time anomalies caused by the stagnant slab. *IUGG XXIV Gen. Assem., Perugia, Italy*, JSS012–2211 (Abstr.)

Tackley PJ, Stevenson DJ, Glatzmaier GA, Schubert G. 1993. Effects of an endothermic phase transition at 670 km depth in a spherical model of convection in the Earth's mantle. *Nature* 361:699–704

Tagawa M. 2007. *Numerical modeling of slab dynamics: history-dependent rheology and slab stagnation mechanisms*. Doc. thesis. Hiroshima Univ., Jpn. 218 pp.

Tagawa M, Nakakuki T, Tajima F. 2007. Dynamical modeling of trench retreat driven by the slab interaction with the mantle transition zone. *Earth Planets Space* 59:65–74

Tarits P, Hautot S, Perrier F. 2004. Water in the mantle: results from electrical conductivity beneath the French Alps. *Geophys. Res. Lett.* 31:L06612

Tetzlaff M, Schmeling H. 2000. The influence of olivine metastability on deep subduction of oceanic lithosphere. *Phys. Earth Planet. Inter.* 120:29–38

Thomas C, Kendall J-M, Lowman J. 2004. Lower-mantle seismic discontinuities and the thermal morphology of subducted slabs. *Earth Planet. Sci. Lett.* 225:105–13

Tono Y, Kunugi T, Fukao Y, Tsuboi S, Kanjo K, Kasahara K. 2005. Mapping of the 410- and 660-km discontinuities beneath the Japanese islands. *J. Geophys. Res.* 110:BO3307

Torii Y, Yoshioka S. 2007. Physical conditions for slab stagnation: constraints from Clapeyron slope, mantle viscosity, trench retreat, and dip angles. *Tectonophysics* 445:200–9

Trampert J, Vacher P, Vlaar N. 2001. Sensitivities of seismic velocities to temperature, pressure and composition in the lower mantle. *Phys. Earth Planet. Inter.* 124:255–67

Tsuchiya T, Tsuchiya J, Umemoto K, Wentzcovitch RM. 2004. Elasticity of postperovskite $MgSiO_3$. *Geophys. Res. Lett.* 31:L14603

Utada H, Goto T, Koyama T, Shimizu H, Obayashi M, Fukao Y. 2005. *Electrical conductivity in the mantle transition zone beneath the northwestern Pacific and its implications for the presence of water*. Presented at AGU Fall Meet., D141A, San Francisco (Abstr.)

van der Hilst RD, Engdahl ER, Spakman W. 1993. Tomographic inversion of P and pP data for aspherical mantle structure below the northwest Pacific region. *Geophys. J. Int.* 115:264–302

van der Hilst RD, Engdahl ER, Spakman W, Nolet G. 1991. Tomographic imaging of subducted lithosphere below northwest Pacific island arcs. *Nature* 353:37–43

van der Hilst RD, Widiyantoro S, Engdahl ER. 1997. Evidence for deep mantle circulation from global tomography. *Nature* 386:578–84

van der Lee S, Nolet G. 1997. Seismic image of the subducted trailing fragments of the Farallon plate. *Nature* 386:266–69

van der Voo R, Spakman W, Bijwaard H. 1999. Mesozoic subducted slabs under Siberia. *Nature* 397:246–49

van Keken PE, Karato S, Yuen DA. 1996. Rheological control of oceanic crust separation in the transition zone. *Geophys. Res. Lett.* 23:1821–24

Wang D, Mookgerjee M, Xu Y, Karato S. 2006. The effect of water on the electrical conductivity of olivine. *Nature* 443:977–80

Wang J, Sinogeikin SV, Inoue T, Bass JD. 2003. Elastic properties of hydrous ringwoodite. *Am. Mineral.* 88:1608–11

Wicks CW Jr, Richards MA. 1993. A detailed map of the 660-km discontinuity beneath the Izu-Bonin subduction zone. *Science* 261:1424–27

Widiyantoro S, Gorbatov A, Kennett BLN, Fukao Y. 2000. Improving global shear wave traveltime tomography using three-dimensional ray tracing and iterative inversion. *Geophys. J. Int.* 141:747–58

Widiyantoro S, Kennett BLN, van der Hilst RD. 1999. Seismic tomography with P and S data reveals lateral variations in the rigidity of deep slabs. *Earth Planet. Sci. Lett.* 173:91–100

Xu Y, Shankland TJ, Poe BT. 2000. Laboratory-based electrical conductivity in the Earth's mantle. *J. Geophys. Res.* 105:27865–75

Yamazaki D, Inoue T, Okamoto M, Irifune T. 2005. Grain growth kinetics of ringwoodite and its implication for rheology of the subducting slab. *Earth Planet. Sci. Lett.* 236:871–81

Yanagisawa T, Yamagishi Y. 2005. Rayleigh-Benard convection in spherical shell with infinite Prandtl number at high Rayleigh number. *J. Earth Simulator* 4:11–17

Yoshioka S, Sanshadokoro H. 2002. Numerical simulations of deformation and dynamics of horizontally lying slabs. *Geophys. J. Int.* 151:69–82

Zhao D. 2004. Global tomographic images of mantle plumes and subducting slabs: insight into deep Earth dynamics. *Phys. Earth Planet. Inter.* 146:3–34

Annual Review
of Earth and
Planetary Sciences

Volume 37, 2009

# Contents

Where Are You From? Why Are You Here? An African Perspective on Global Warming
*S. George Philander* ..... 1

Stagnant Slab: A Review
*Yoshio Fukao, Masayuki Obayashi, Tomoeki Nakakuki, and the Deep Slab Project Group* ..... 19

Radiocarbon and Soil Carbon Dynamics
*Susan Trumbore* ..... 47

Evolution of the Genus *Homo*
*Ian Tattersall and Jeffrey H. Schwartz* ..... 67

Feedbacks, Timescales, and Seeing Red
*Gerard Roe* ..... 93

Atmospheric Lifetime of Fossil Fuel Carbon Dioxide
*David Archer, Michael Eby, Victor Brovkin, Andy Ridgwell, Long Cao, Uwe Mikolajewicz, Ken Caldeira, Katsumi Matsumoto, Guy Munhoven, Alvaro Montenegro, and Kathy Tokos* ..... 117

Evolution of Life Cycles in Early Amphibians
*Rainer R. Schoch* ..... 135

The Fin to Limb Transition: New Data, Interpretations, and Hypotheses from Paleontology and Developmental Biology
*Jennifer A. Clack* ..... 163

Mammalian Response to Cenozoic Climatic Change
*Jessica L. Blois and Elizabeth A. Hadly* ..... 181

Forensic Seismology and the Comprehensive Nuclear-Test-Ban Treaty
*David Bowers and Neil D. Selby* ..... 209

How the Continents Deform: The Evidence from Tectonic Geodesy
*Wayne Thatcher* ..... 237

The Tropics in Paleoclimate
*John C.H. Chiang* ..... 263

Rivers, Lakes, Dunes, and Rain: Crustal Processes in Titan's Methane Cycle
*Jonathan I. Lunine and Ralph D. Lorenz* ..... 299

Planetary Migration: What Does it Mean for Planet Formation?
*John E. Chambers* ..... 321

The Tectonic Framework of the Sumatran Subduction Zone
*Robert McCaffrey* ..... 345

Microbial Transformations of Minerals and Metals: Recent Advances in Geomicrobiology Derived from Synchrotron-Based X-Ray Spectroscopy and X-Ray Microscopy
*Alexis Templeton and Emily Knowles* ..... 367

The Channeled Scabland: A Retrospective
*Victor R. Baker* ..... 393

Growth and Evolution of Asteroids
*Erik Asphaug* ..... 413

Thermodynamics and Mass Transport in Multicomponent, Multiphase $H_2O$ Systems of Planetary Interest
*Xinli Lu and Susan W. Kieffer* ..... 449

The Hadean Crust: Evidence from >4 Ga Zircons
*T. Mark Harrison* ..... 479

Tracking Euxinia in the Ancient Ocean: A Multiproxy Perspective and Proterozoic Case Study
*Timothy W. Lyons, Ariel D. Anbar, Silke Severmann, Clint Scott, and Benjamin C. Gill* ..... 507

The Polar Deposits of Mars
*Shane Byrne* ..... 535

Shearing Melt Out of the Earth: An Experimentalist's Perspective on the Influence of Deformation on Melt Extraction
*David L. Kohlstedt and Benjamin K. Holtzman* ..... 561

**Indexes**

Cumulative Index of Contributing Authors, Volumes 27–37 ..... 595

Cumulative Index of Chapter Titles, Volumes 27–37 ..... 599

**Errata**

An online log of corrections to *Annual Review of Earth and Planetary Sciences* articles may be found at http://earth.annualreviews.org